Dijet studies with ALICE at the LHC

Master's thesis, 6.5.2018

Author:

Oskari Saarimäki

Supervisors:

Sami Räsänen

Dong Jo Kim

UNIVERSITY OF JYVÄSKYLÄ

Tiivistelmä

Saarimäki, Oskari
Dijettitutkimus ALICE-kokeelle LHC-kiihdyttimessä.
Pro Gradu -tutkielma
Fysiikan laitos, Jyväskylän yliopisto, 2018, 66 sivua

Relativistisissa hiukkastörmäyksissä syntyvistä suurenergisistä kvarkeista ja gluoneista, eli partoneista, muodostuvaa hyvin kollimoitunutta hiukkassuihkua kutsutaan jetiksi. Jettien tutkimusta on tehty jo vuosikaudet ja se hallitaan hyvin myös raskasionitörmäyksissä, joissa muodostuvaa kvarkkigluoniplasmaa on pystytty tutkimaan jettien liikemäärähäviöiden avulla. Tämän perusteella on huomattu, että kvarkkigluoniplasma jarruttaa sen läpi kulkevia suurenergisiä partoneita. Jettien lisäksi partonien energiahäviöitä raskasionitörmäyksessä on tutkittu myös dijettien avulla. Dijetti on määritelty törmäyksen kahdesta suurimman energian omaavasta jetistä muodostuvaksi systeemiksi. Aiempien RHIC- ja LHC-kiihdyttimistä saatujen tulosten perusteella nähdään, että dijetin invariantti massa voi olla herkkä raskasionitörmäyksissä muodostuvan kvarkkigluoniplasman aiheuttamille muutoksille, mikä antaa vahvan motivaation aiheen tutkimiselle.

Tässä pro gradu -tutkielmassa esitän ensimmäiset tulokset dijettien massajakaumista protoni–lyijy- ja lyijy–lyijy-törmäyksissä massakeskipiste-energialla $\sqrt{s_{\mathrm{NN}}} = 5{,}02$ TeV ALICE-kokeelle LHC-kiihdyttimellä. Työssäni olen rekonstruoinut jetit varatuista hiukkasista käyttäen anti-k_{T} jettialgoritmia resoluutioparametrilla $R = 0{,}4$. Tulosteni mukaan protoni–lyijy-törmäyksissä dijetin massan muutokset verrattuna protoni–protoni-törmäyksiin ovat merkityksettömiä. Vertaamalla lyijy–lyijy-tuloksia protoni–lyijy-tuloksiin näkyy keskeisissä lyijy–lyijy-törmäyksissä mahdollinen muutos yli 100 GeV:n dijetin massan alueella.

Kokeessa osa hiukkasista jää havaitsematta, ja havaittujenkin hiukkasten liikemäärä mitataan äärellisellä resoluutiolla. Tämän vuoksi käsittelemätön data täytyy korjata ilmaisimesta johtuvien epäfysikaalisten efektien huomioimiseksi, ja sitä varten käytetään niin kutsuttua unfolding-menetelmää. Tässä työssä esitän tällä menetelmällä korjatut tulokset protoni–lyijy-tapauksessa. Lyijy–lyijy-törmäysten unfolding-menetelmä on vielä kehityksen alla.

Avainsanat: opinnäyte, relativistinen raskasionitörmäys, energiahäviö, jettien rekonstruktio, dijetin massa, ALICE, LHC, CERN

Abstract

Saarimäki, Oskari
Dijet studies with ALICE at the LHC
Master's thesis
Department of Physics, University of Jyväskylä, 2018, 66 pages.

High energy partons, quarks and gluons, born in relativistic particle collisions create well collimated showers of particles, which are called jets. Jets have been studied for years, and also used widely in heavy ion collisions, where the quark-gluon plasma (QGP) medium forms. Studying jets in heavy ion collisions showed that hard partons lose energy in the QGP medium. Hard parton energy loss has also been studied with dijets. A dijet is a system consisting of two of the most energetic jets in a collision. Previous studies from RHIC and LHC indicate that dijet invariant mass can be sensitive to modifications caused by the QGP medium.

In this thesis I present the first measurements of dijet mass distributions in proton–lead and lead–lead collisions at $\sqrt{s_{\mathrm{NN}}} = 5.02$ TeV with the ALICE detector at the LHC. In this work, I have reconstructed jets from charged particles using the anti-k_{T} jet reconstruction algorithm with resolution parameter $R = 0.4$. According to my results, the proton–lead collisions show negligible modification in the dijet mass distribution compared to the proton–proton Monte Carlo simulation results. Comparing the lead–lead results to proton–lead shows possible modifications in the high dijet mass region over 100 GeV.

In the experiment some amount of the particles produced are lost to detector inefficiencies. The raw data can be corrected for the inefficiencies, and this procedure is called unfolding. In this thesis I show the unfolded spectra of the proton–lead data, but the lead–lead unfolding needs to be developed so that the jets lost because of the background subtraction get corrected as well.

Keywords: thesis, relativistic heavy ion collisions, energy loss, jet reconstruction, dijet mass, ALICE, LHC, CERN

Contents

1 Introduction

Quarks and gluons are the elementary particles that form protons, neutrons and other hadrons. Partons, which quarks and gluons are together called, cannot appear alone because of the color confinement. There are three colors for quarks, three anticolors for antiquarks, and a total of eight possible combinations of color and anticolor pairs for gluons [1, p.280]. The Standard Model of particle physics predicts that in extremely high temperatures and densities, the color confinement of the quarks can be temporarily broken in an exotic state of matter called the Quark Gluon Plasma (QGP) [2, 3]. These conditions are thought to have been present in the early stages of our universe, where parton density and temperature were so high that the partonic matter of the whole universe was in the QGP state [3]. After some tens of microseconds after the Big Bang the expansion of the universe made matter cool and sparsely distributed enough for partons to be confined within hadrons. In figure 1 the phase diagram of Quantum Chromodynamic (QCD) matter is drawn, and there one can see how the hadronic matter transforms into the QGP when temperature is over 150 MeV, which corresponds to about 1.74×10^{12} Kelvin. The net baryon density is zero for a system with equal amounts of partons and antipartons, and positive for matter with more partons than antipartons. For example during the early universe the net baryon density was almost negligible, but non-zero [4]. In our time, there are models which point that quark-gluon matter is created naturally in some heavy neutron stars and supernova explosions [5, 6]. The matter in neutron stars is described as a cool quark matter, and it would be positioned in the phase diagram somewhere with high net baryon density and low temperature [7].

In laboratory, QGP is being produced in ultrarelativistic heavy ion collisions in the Relativistic Heavy Ion Collider (RHIC) [10, 11] and in the Large Hadron Collider (LHC). In the phase diagram, LHC and RHIC both create a substance with high temperature, over 150 MeV, and baryochemical potential of zero within a margin of error for LHC, and approximately 20 MeV for RHIC [12], which are similar conditions as in the early universe. In figure 2 the various stages of a heavy ion collision are drawn. The primary interactions between colliding nucleons form a dense partonic system. The quarks and gluons are expected to reach thermal equilibrium and the system is dense enough to reach the QGP phase [13]. Evolution of this system can be described by hydrodynamic calculations [14]. As the system expands and cools down, partons hadronize when the temperature drops below the critical temperature of $T_c \sim 150$ MeV. The secondary interactions freeze out when the system gets sparse, and particles stream freely towards the detectors. Some short-lived resonances decay before they reach the detectors. The lifetime of the system from the beginning till the hadronization is approximately 15 fm/$c = 5 \times 10^{-23}$ seconds [15].

As the lifetime of the QGP in relativistic heavy ion collisions is extremely small, probes which are born inside the system are used, for example photons, dileptons, and hard partons. Photons and dileptons, which interact electromagnetically and do not feel the strong force, have a mean free path of approximately 500 fm in QGP medium [16]. This means that in a head-on heavy ion collision, which creates a volume of QGP with a diameter of approximately 10 fm, electromagnetic particles propagate out of the medium usually without any interaction. Hard partons on the other hand, consisting of quarks or gluons, feel the strong force and interact with the medium strongly. However as the hard parton has so much more kinetic energy compared to the thermalized partons, the hard parton only loses some of the energy to the medium but does not thermalize. This energy loss of the parton can be used to study the QGP, and is generally called the jet quenching [17]. Partons that have high enough energy can punch through the plasma and hadronize in the vacuum [18]. The hadrons formed from a high energy parton are well collimated in a shower called a jet. Figure 3 shows schematically the hadronization of a high energy parton hadronizes, which is then detected as a jet in the detector system.

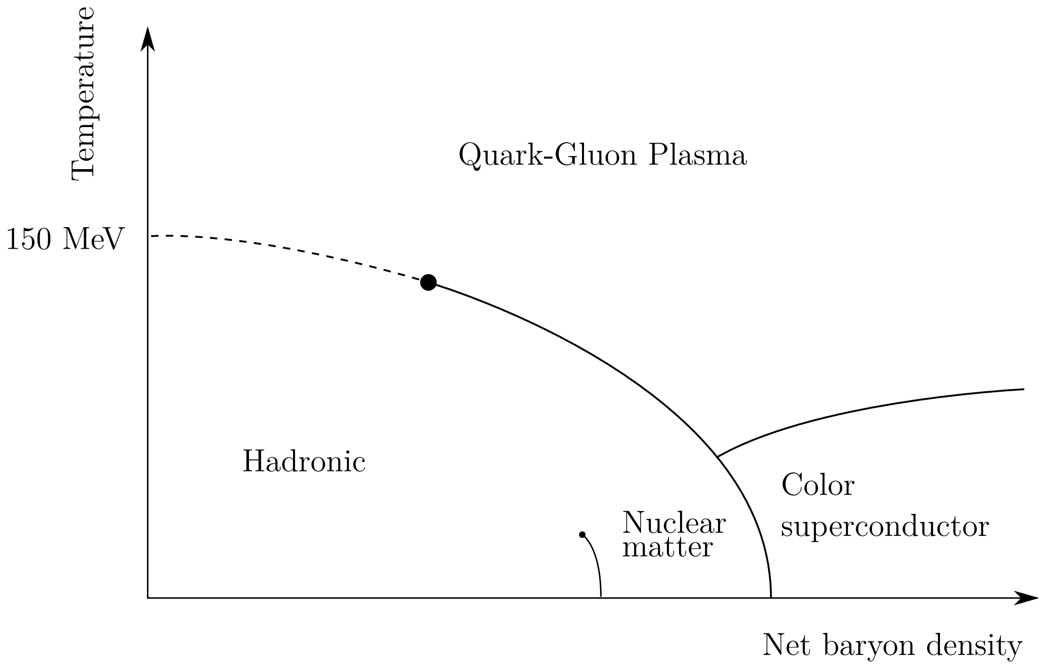

Figure 1. Phase diagram of QCD matter. Solid lines represent a first order transition, and dots at the end of lines represent critical points. The dashed line is a smooth crossover from QGP to hadronic matter and vice versa. Nuclear matter refers to normal atomic nucleus conditions. [2, 8]

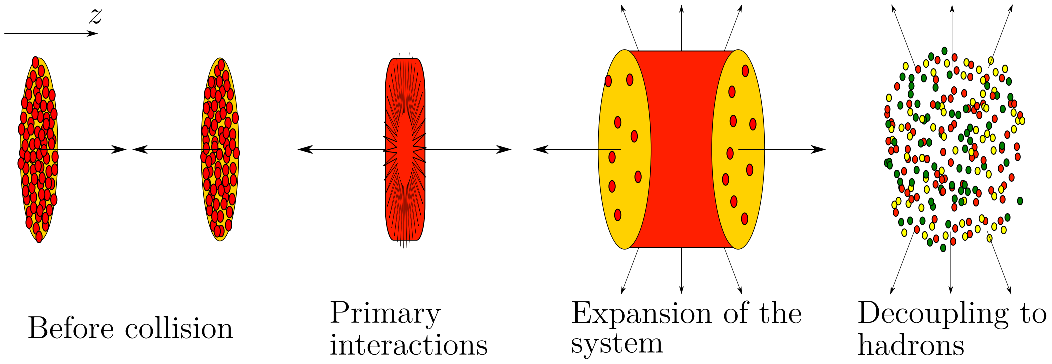

Figure 2. A schematic figure of the various stages of a heavy ion collision. The usual convention is to use the beam axis as the z axis and x-y plane as the transverse plane.

Jet quenching studies started first as a two-particle correlation studies at RHIC [19]. The idea is to measure azimuthal angles between the most energetic particle and other particles, where the azimuthal angle is the angle in transverse plane of the collision. This is an interesting quantity because if the initial transverse momentum of the system is small, then hard partons born in the system should have back-to-back pairs because of the conservation of momentum. An example of such a hard process is gluon–gluon to gluon–gluon scattering, which is drawn in figure 4, and it is one of the most dominant reactions in a high energy hadron collisions. The most energetic parton of an event is called leading parton, and similarly the second most energetic parton is called subleading parton. The leading parton creates the near-side jet, which has an away-side jet pair born from the subleading parton. These leading and subleading jets are then seen in the two-particle correlation figures as peaks and as such, can be studied.

It has been studied that in heavy ion collisions energetic partons, which are detected as jets, are born near the surface of the collision zone [18]. In figure 5 the main results

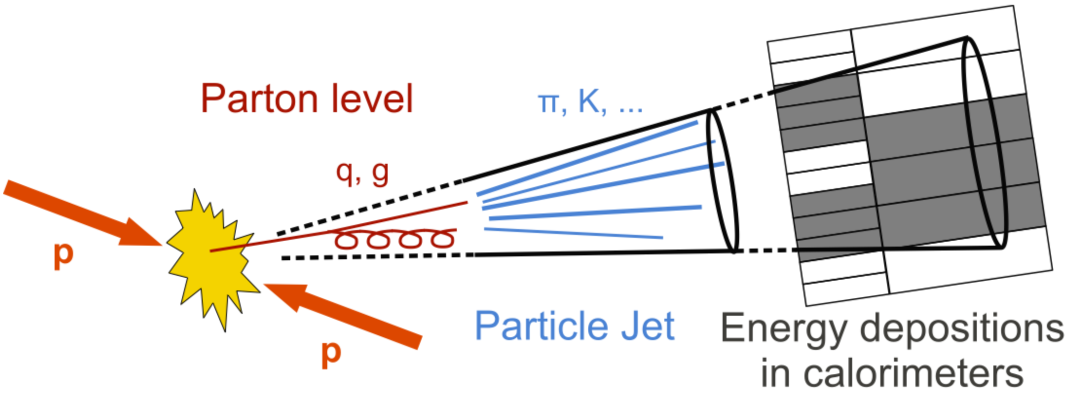

Figure 3. A jet born from a high energy parton in a proton–proton collision. The figure source [9].

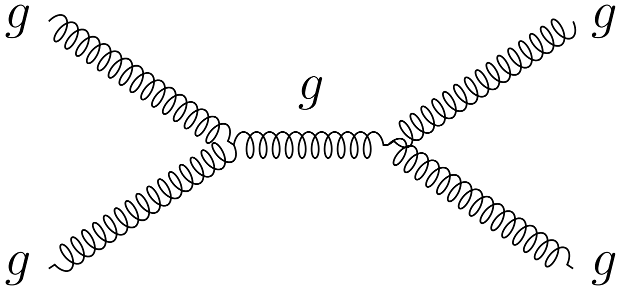

Figure 4. A Feynman diagram depicting a gluon–gluon to gluon–gluon interaction.

are seen for two different triggers. First trigger requires a near-side hadron detection with 8 GeV $< p_{\mathrm{T}} <$ 15 GeV transverse momentum, and second trigger requires in addition to that an away-side hadron detection with 4 GeV $< p_{\mathrm{T}} <$ 6 GeV transverse momentum. On the left side of the figure 5, the surface bias of the parton production vertex is clearly seen. As the parton always propagates to $-x$ direction in these figures, partons produced on the other side lose so much energy for the medium that the event is not triggered. In the right side figure, the parton production vertex is much more plausible to be found in the center of the collision zone. This is natural as the trigger requires also an energetic away-side hadron, so a punchthrough for both partons needs to happen. These calculations show that a single jet might not be modified by the medium that much because of the surface bias, but detecting both leading and subleading jet guarantees that at least one of the partons have propagated a significant length in the medium. The suppression of the away-side jet has been seen by the STAR collaboration at the RHIC [19]. In the STAR results, the near-side jet is almost unchanged in proton–proton, deuteron–gold and gold–gold systems, but the away-side jet has been modified heavily in the heavy ion collisions. This indicates a strong attenuation of the away-side parton energy in the medium.

Ideally the jet could be reconstructed completely by catching all the particles created in the hadronization of the original parton. Even though this cannot be most of the time done perfectly, there are several different algorithms for reconstructing a jet in a way that particles that are grouped together get added up as a jet, and the summed up momentum of the jet constituents is comparable to the initial hadronized parton momentum. Jets in electron–positron and proton–proton collisions can be reconstructed almost completely as the underlying event is so small, where underlying event refers to everything else besides the primary hard scattering. In figure 6a two jets back-to-back of each other are created in a proton–proton collision, and both of the jets can clearly be seen. For comparison, in figure 6b a similar event with two jets has been recorded in a lead–lead collision. Here both jets are seen as well, but the subleading jet has seemingly almost completely melted to the background.

There have been studies to use single-jet invariant mass as a probe in heavy ion

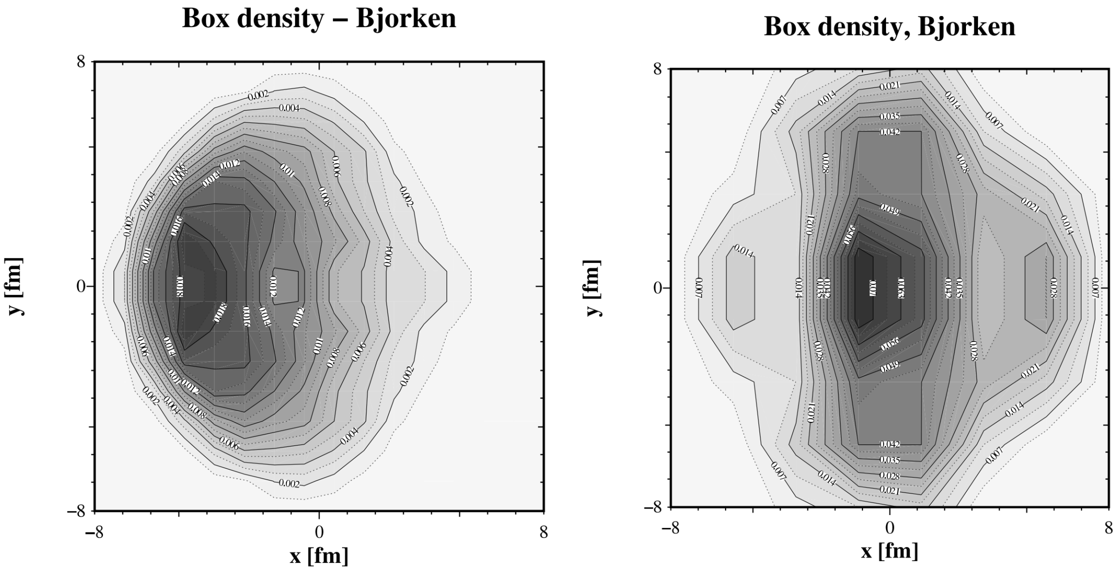

Figure 5. Probability density for finding a hard scattering vertex at (x,y). In the left figure the event is triggered if the leading hadron has a transverse momentum of 8 GeV< p_{T} < 15 GeV, and on the right figure in addition to that, an away-side hadron with transverse momentum 4 GeV < p_{T} < 6 GeV is required. In every event the leading hadron propagates to the $-x$ direction. [18]

collisions. Where the invariant mass is defined to be $M^2 = E^2 - p_{\mathrm{T}}^2 - p_z^2$, where E is the energy, p_{T} the transverse momentum and p_z longitudinal momentum of the jet [21]. Theoretically there are signs that the jet mass would be affected in the heavy ion collision [22], but in an experimental study the systematic error was so large that no definitive conclusion could be made [21].

The observed imbalance between near and away-side jets gives motivation to study a system of the two most energetic jets, which together are called a dijet. ATLAS and CMS experiments have studied the momentum imbalance between the dijet partners [23, 24], which agree that the imbalance does indeed grow in central collisions. In this work, I propose to study modifications in the invariant mass of the dijet system in the proton–lead and lead–lead collisions, as compared to proton–proton collisions. Dijet mass has been studied in proton–proton collisions by ATLAS [25] and CMS [26], but not in any larger systems yet. The modification of the away-side jet observed by STAR [19] and the results for the dijet energy imbalance by ATLAS and CMS [23, 24] indicate that also the dijet mass could well be affected by the jet energy loss. As the dijet mass has not yet been studied in a heavy ion environment, this study could provide a new method for studying the QGP.

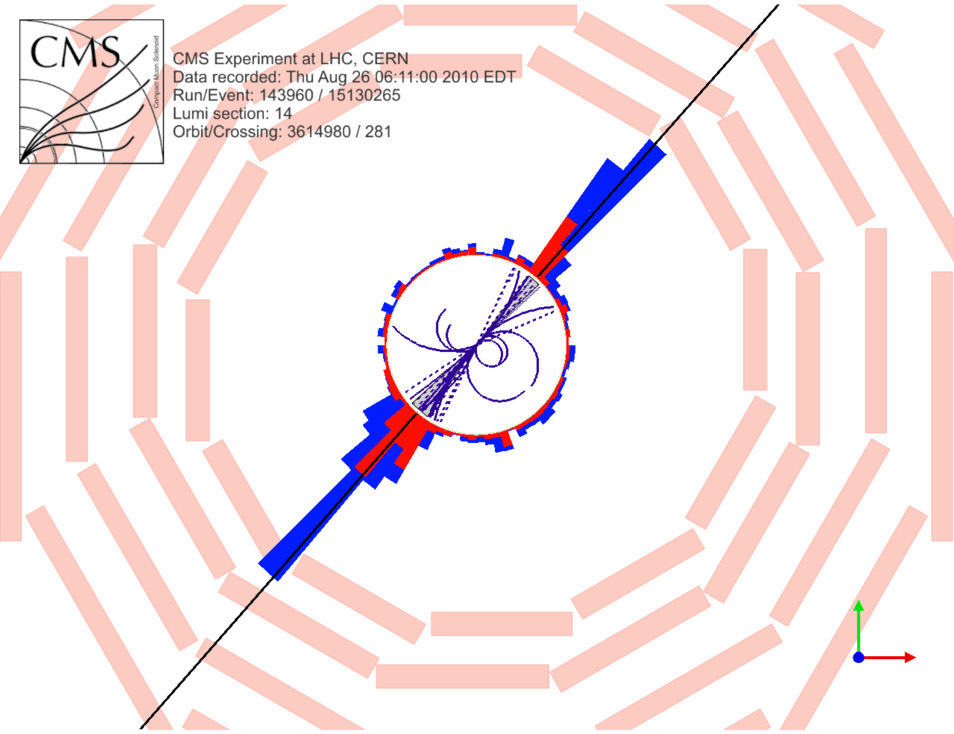

(a) Proton–proton collision. Figure source: [20]

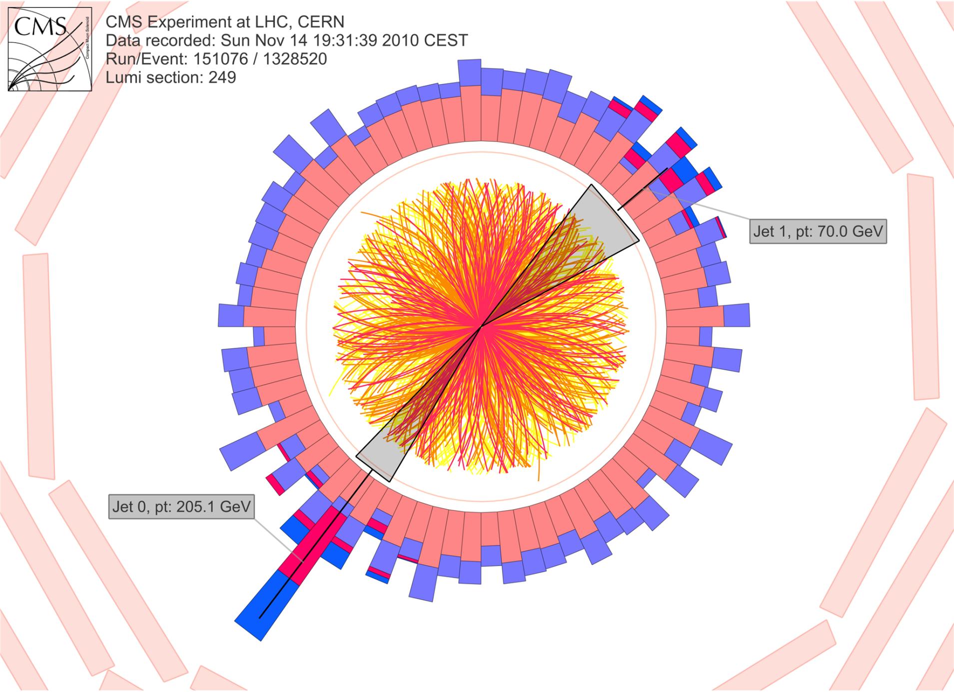

(b) Lead–lead collision.

Figure 6. An example of a dijet born in a proton–proton collision and a heavy ion collision measured by the CMS experiment. One can easily note how big a difference there is in the underlying event between proton–proton collisions and heavy ion collisions. The subleading jet in the heavy ion case has almost melted in the background.

2 Theoretical background

2.1 Nuclear modification factor

In order to study the modifications of spectra caused by the QGP medium in heavy ion collisions, RHIC experiments PHENIX and STAR started to a measure nuclear modification factor [10, 11] defined as

$$R_{\mathrm{AA}}\left(p_{\mathrm{T}}\right)=\frac{\frac{\mathrm{d}N_{\mathrm{AA}}^{2}}{\mathrm{d}p_{\mathrm{T}}\mathrm{d}\eta}\left(p_{\mathrm{T}}\right)}{\left\langle N_{\mathrm{coll}}\right\rangle\frac{\mathrm{d}N_{\mathrm{pp}}^{2}}{\mathrm{d}p_{\mathrm{T}}\mathrm{d}\eta}\left(p_{\mathrm{T}}\right)}=\frac{\frac{\mathrm{d}N_{\mathrm{AA}}^{2}}{\mathrm{d}p_{\mathrm{T}}\mathrm{d}\eta}\left(p_{\mathrm{T}}\right)}{\left\langle T_{\mathrm{AA}}\right\rangle\frac{\mathrm{d}\sigma_{\mathrm{pp}}^{2}}{\mathrm{d}p_{\mathrm{T}}\mathrm{d}\eta}\left(p_{\mathrm{T}}\right)},\tag{1}$$

where $\left\langle T_{\mathrm{AA}}\right\rangle=\left\langle N_{\mathrm{coll}}\right\rangle/\sigma_{\mathrm{inel}}^{pp}$, and $\sigma_{\mathrm{inel}}^{pp}$ is the proton–proton total inelastic cross section. The proton–proton yield is multiplied with the average number of binary collisions $\left\langle N_{\mathrm{coll}}\right\rangle$, that is the amount of independent nucleon–nucleon collisions in a single heavy ion collision. I will discuss the determination of N_{coll} in section 2.5. If there were no medium effects in a heavy ion collision $R_{\mathrm{AA}}=1$. This would mean that a heavy ion collision would be indistinguishable from a sum of independent nucleon–nucleon collisions. Figure 7 shows the nuclear modification factor measured by the STAR collaboration at RHIC on left and various experiments at the LHC on right. In the LHC results R_{CP} is used instead of R_{AA}. Both are similar, except in R_{CP} different centrality classes are compared against each other, instead of comparing to proton–proton collisions. In these figures the percentiles represent the centrality of a collision, the smaller it is the more central the collision is. More details on centrality are presented in section 2.5. The results show that the nuclear modification factor approaches one in the peripheral collisions at high transverse momentum region that is dominated by hard physics. This is in accordance with the intuition that the medium is largest in central collisions and when shifting towards more peripheral collisions, the system size gets smaller and QGP is no longer formed. Similar studies show also that the minimum bias proton–lead collision does not get modified [27]. On the other hand, recent studies indicate that QGP might be formed in very high multiplicity proton–lead [28, 29] or even proton–proton [30] collisions. These high multiplicity proton–lead and proton–proton events are so rare that they do not affect the minimum bias results for hard probes.

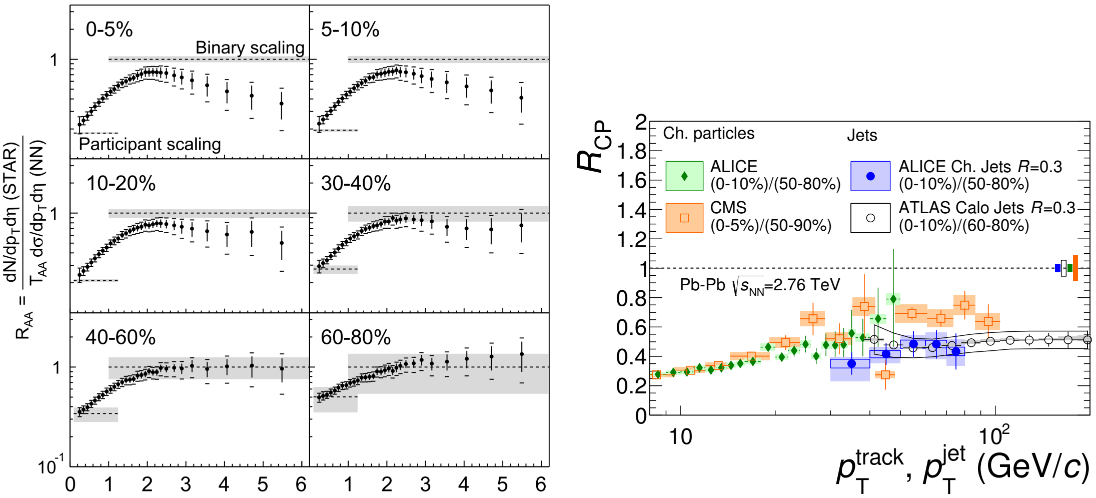

(a) STAR collaboration nuclear modification factor results for charged particles [11]. STAR compared a gold–gold system to proton–proton. The shaded regions represent the systematic uncertainties of the result.

(b) Comparison of ALICE, CMS and ATLAS R_{CP} results for a lead–lead system [31]. Here, in addition to particle R_{CP}, also jet R_{CP} are shown.

Figure 7. Nuclear modification factor studies at RHIC and LHC.

2.2 Single inclusive hadron distributions

The high transverse momentum particle production can be described theoretically with the use of collinear factorization. Perturbative QCD is used to calculate cross sections of short distance interactions, but long distance effects need to be taken into account via other means as pQCD is not applicable. This means that when calculating hadron yields in a collision, in addition to the perturbative cross section, also initial parton distributions and parton fragmentation functions are needed. The production cross section of a high transverse momentum hadron h can be written as

$$\mathrm{d}\sigma^{\mathrm{hard}}_{pp\to h} = \sum_{a,b,c} f_a\left(x_1,Q^2\right) \otimes f_b\left(x_2,Q^2\right) \otimes \mathrm{d}\sigma^{\mathrm{hard}}_{ab\to cX}\left(x_1,x_2,Q^2\right) \otimes \mathscr{D}_{c\to h}\left(z,Q^2\right), \quad (2)$$

where $f_a\left(x,Q^2\right)$ is the parton distribution function (PDF), representing the probability density of finding a parton of flavor a inside a nucleus with a fraction $x = p_{\mathrm{parton}}/p_{\mathrm{nucleus}}$ of the original nucleus momentum, $\mathrm{d}\sigma^{\mathrm{hard}}_{ab\to cX}\left(x_1,x_2,Q^2\right)$ is the perturbative cross section between the partons a and b, forming parton c and any particles X, $\mathscr{D}_{c\to h}\left(z,Q^2\right)$ is the parton–hadron fragmentation function which describes the probability density of the outgoing parton c to hadronize into a final hadron h with momentum fraction $z = p_{\mathrm{hadron}}/p_{\mathrm{parton}}$ [17]. The perturbative cross section can be calculated theoretically with the help of Feynman diagrams like in figure 4. PDFs and fragmentation functions cannot be calculated using perturba-

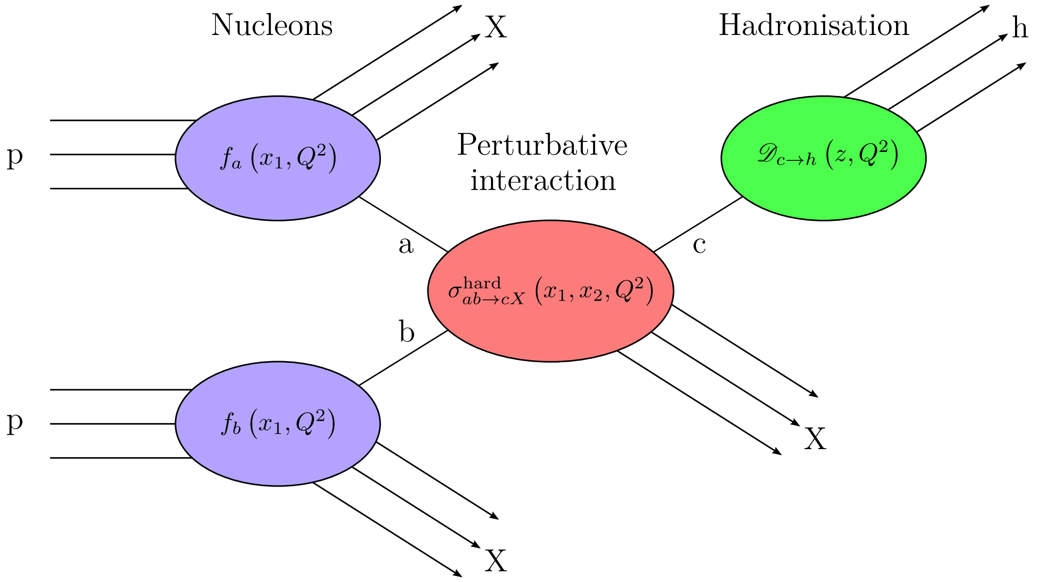

Figure 8. In this figure, different parts of the hadronic yield of formula 2 are shown visually.

tion theory, so they combine theory and phenomenology. The equation 2 can be visually presented as in figure 8, where PDFs describe the initial nucleus, perturbative cross section handles the underlying perturbative theory and fragmentation functions handle the hadronization.

In order to take nuclear effects and medium into account for heavy ion collisions, equation 2 needs to be modified. The PDFs are changed from free proton PDFs into corresponding PDFs of a nucleon bound in atomic nucleus, and the fragmentation functions are modified as

$$\mathscr{D}^{\text{med}}_{c\rightarrow h}\left(z', \hat{q}, Q^2\right) = P\left(\varepsilon, \hat{q}\right) \otimes \mathscr{D}^{\text{vac}}_{c\rightarrow h}\left(z, Q^2\right), \tag{3}$$

where $P\left(\varepsilon, \hat{q}\right)$ is called a quenching weight. It describes the probability that the parton in question loses a fraction of energy $\varepsilon = \Delta E/E$ due to the medium. The transport coefficient $\hat{q}$ describes the scattering power of a medium. Typically [17] the parton energy loss $\Delta E \propto \langle\hat{q}\rangle L^2$, where $\langle\hat{q}\rangle$ is an average transport coefficient, and L is the path length of a parton propagating inside the medium. There are several models aiming for constraining the $\langle\hat{q}\rangle$, such as the AMY or BDMPS models, which are named by their authors Arnold, Moore and Yaffe, and Baier, Dokshitzer, Mueller, Peigné and Schiff. The modifications for equation 2 are needed as the medium traversing parton radiates gluons which affect the resulting hadrons. This is illustrated in figure 9. Medium-modified fragmentation functions typically have an enhancement in the low z region, and depletion in the high z region, which is natural as the maximum momentum of the final hadron is reduced when the original parton loses energy radiating soft gluons [32].

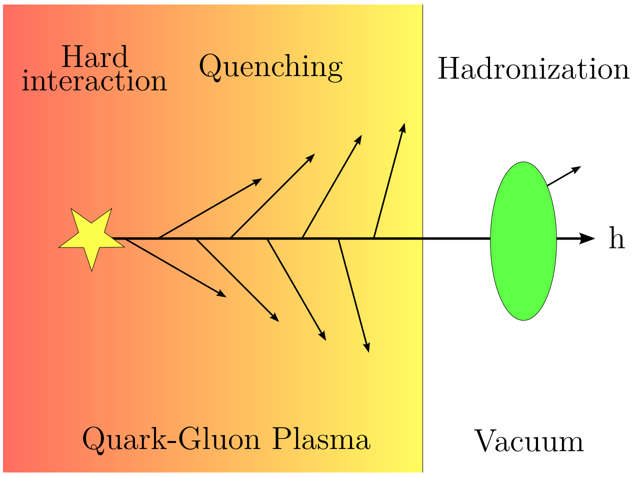

Figure 9. Medium interacting with a parton, modifying its energy.

With the help of equation 2 hadron yield in proton–proton collisions can be calculated theoretically in. The medium-modified version of the equation is then used to calculate heavy ion collision hadron yield. By combining these calculations, R_{AA} can be calculated theoretically with different models and parameters. Tuning the model parameters, like $\hat{q}$, so that they fit into data gives possible restrictions to said parameters. For example comparing theory with RHIC results, the transport coefficient was estimated to be in the ballpark of $\hat{q} \sim$ 5–15 $\mathrm{GeV}^2/\mathrm{fm}$ by [33].

2.3 Jet cross section

Jets originate from the hard partons which fragment in vacuum. Ideally one could recombine the jet constituents in a way that the original four-vector of the parton could be recovered, and as such undo the fragmentation process. With this in mind, the jet production cross section would actually be the partonic production cross section, which is as in equation 2 except without fragmentation functions

$$\mathrm{d}\sigma^{\mathrm{parton}}_{pp\to k} = \sum_{a,b} f_a\left(x_1,Q^2\right) \otimes f_b\left(x_2,Q^2\right) \otimes \mathrm{d}\sigma^{\mathrm{hard}}_{ab\to kX}\left(x_1,x_2,Q^2\right). \tag{4}$$

The partonic production cross section would be a lot cleaner than hadronic production cross section because non-perturbative parts other than the PDFs are not needed in this calculation. The closest this has been reached has been probably in $e^+ + e^- \to q + \bar{q} \to \mathrm{jet} + \mathrm{jet}$ reactions, which are so clean that the individual jet constituents can be summed up. Proton–proton collisions like in figure 6a are also quite clean, but already there the underlying event [34] born for example from multiparton interactions and various QCD radiation processes, starts to make the analysis more complicated.

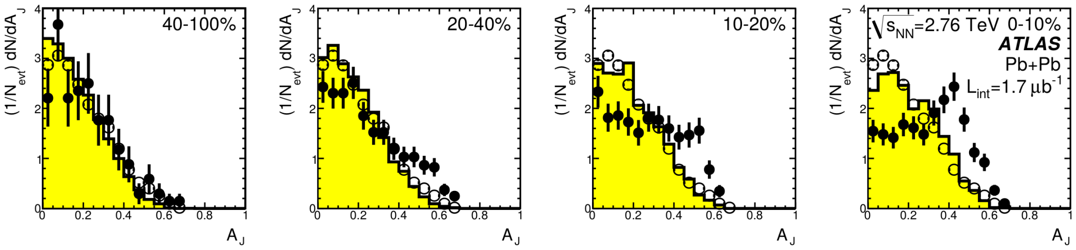

Figure 10. Dijet energy imbalance results of the ATLAS experiment [23]. Full circles are lead–lead results, open circles are proton–proton results and the yellow histogram is HIJING + Pythia MC results.

2.4 Dijet energy imbalance

The leading and subleading jets generally have different path lengths in the medium, which would mean that the energy loss of the leading and the subleading jet is uneven. As the leading and subleading jets initially have approximately the same energy, the uneven energy loss creates an energy imbalance in the dijet system. This energy imbalance was observed by ATLAS [23] and CMS [24] measurements that studied the dijet energy imbalance

$$A_{\mathrm{J}} = \frac{E_{\mathrm{T},1} - E_{\mathrm{T},2}}{E_{\mathrm{T},1} + E_{\mathrm{T},2}} \text{ for all dijets where } \Delta\varphi > \frac{\pi}{2}, \tag{5}$$

where $E_{\mathrm{T}} = p_{\mathrm{T}}^2 + m^2$ is the transverse energy, and $\Delta\varphi \in [0,\pi]$ signifies the azimuthal angle between the two jets. Results obtained by ATLAS are presented in figure 10, where the energy imbalance in lead–lead collisions is compared to proton–proton results in several different centrality bins. The heavy ion and proton–proton results agree in the most peripheral bin, but the difference grows towards more central collisions. This energy imbalance in heavy ion collisions indicates that also the dijet mass studied in this thesis could very well be modified by the medium.

2.5 Centrality in heavy ion collisions

Centrality of a heavy ion collision is highly tied to the geometry of the collision. It is most usually described with impact parameter b, which is the distance between the centers of two nuclei. For an exactly central collision the impact parameter would be zero and, in the hard sphere approximation for the nucleus, up to the maximum distance of twice the nuclear radius. For example in figure 11 the impact parameter is approximately 7 fm. Naturally as the impact parameter gets smaller, the collision zone grows bigger, thus creating a bigger medium. This conclusion is in a good agreement with the nuclear modification factor results from the STAR collaboration in figure 7a, and various other experiment at the LHC in figure 7b, and also in the ATLAS experiment A_{J} results in figure 10.

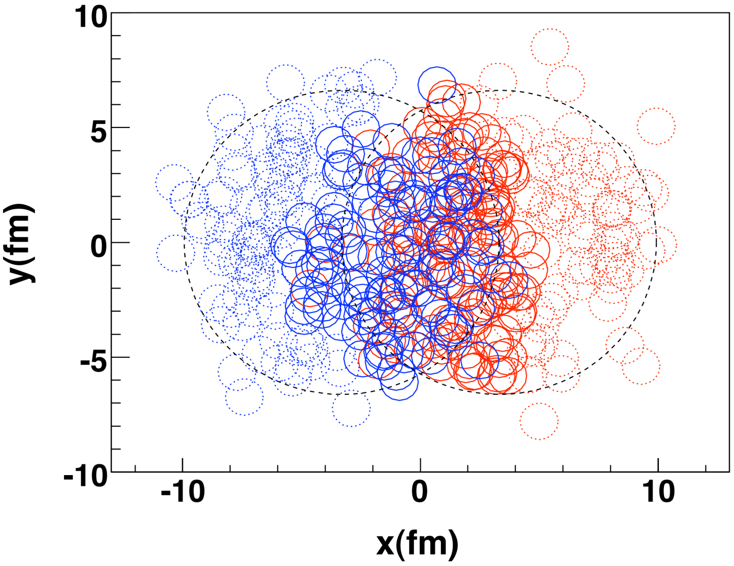

Figure 11. Typical Glauber model Monte Carlo event for lead–lead collision [35]. Here the nuclei are travelling in opposite longitudinal directions and colliding peripherally. The nucleons which do not interact in a heavy ion collision are called *spectators*, and are drawn with dashed circles. Nucleons which do interact are called *participants*, and are drawn with solid circles.

In the figures presented previously, the centrality has been always shown as a percentile, instead of using the impact parameter. This is only natural as the impact parameter is not something that can be measured in experiments. Centrality percentile is defined to be

$$c = \frac{\int_0^b \frac{\mathrm{d}\sigma}{\mathrm{d}b'}\mathrm{d}b'}{\int_0^\infty \frac{\mathrm{d}\sigma}{\mathrm{d}b'}\mathrm{d}b'} = \frac{1}{\sigma_{\mathrm{AA}}}\int_0^b \frac{\mathrm{d}\sigma}{\mathrm{d}b'}\mathrm{d}b' \tag{6}$$

where σ_{AA} is the total production cross section for nucleus collisions.

For example for $0 - 10$ % centrality range minimum is of course $b = 0$ and maximum b_1 can be calculated by solving

$$0.10 = \frac{1}{\sigma_{\mathrm{AA}}}\int_0^{b_1} \frac{\mathrm{d}\sigma}{\mathrm{d}b'}\mathrm{d}b' \tag{7}$$

for b_1. Other ranges can be solved iteratively. For example after solving b_1 previously it is also the minimum impact parameter for the 10–20 % range, and the maximum,

Table 1. Results for MC Glauber calculations for lead–lead collisions in several different centrality classes. Taken from [36].

Centrality (%)	b_{min} (fm)	b_{max} (fm)	$\langle N_{\mathrm{part}}\rangle$	$\langle N_{\mathrm{coll}}\rangle$	$\langle T_{\mathrm{AA}}\rangle$ (1/mb)
0–5	0.00	3.50	382.7	1685	26.32
5–10	3.50	4.94	329.4	1316	20.56
10–20	4.94	6.98	260.1	921.2	14.39
20–40	6.98	9.88	157.2	438.4	6.850
40–60	9.88	12.09	68.56	127.7	1.996
60–80	12.09	13.97	22.52	26.71	0.4174
80–100	13.97	20.00	5.604	4.441	0.06939

b_2 can be solved from

$$0.20 = \frac{1}{\sigma_{\mathrm{AA}}}\int_0^{b_2}\frac{\mathrm{d}\sigma}{\mathrm{d}b'}\mathrm{d}b' = \frac{1}{\sigma_{\mathrm{AA}}}\left(\int_0^{b_1}\frac{\mathrm{d}\sigma}{\mathrm{d}b'}\mathrm{d}b' + \int_{b_1}^{b_2}\frac{\mathrm{d}\sigma}{\mathrm{d}b'}\mathrm{d}b'\right) = 0.10 + \frac{1}{\sigma_{\mathrm{AA}}}\int_{b_1}^{b_2}\frac{\mathrm{d}\sigma}{\mathrm{d}b'}\mathrm{d}b' \tag{8}$$

$$0.10 = \frac{1}{\sigma_{\mathrm{AA}}}\int_{b_1}^{b_2}\frac{\mathrm{d}\sigma}{\mathrm{d}b'}\mathrm{d}b'. \tag{9}$$

As the impact parameter cannot be measured, it is necessary to have a quantity which can be measured and is comparable to the impact parameter b. One such a quantity would be the multiplicity of the event. The corresponding multiplicity for a certain impact parameter can be calculated using a Monte Carlo (MC) method called the Glauber model [36]. In the model ions are simulated by sampling the positions of the nucleons of the ion from the distribution $4\pi r^2\rho(r)$, where $\rho(r)$ is the modified Woods-Saxon distribution

$$\rho(r) = \rho_0\frac{1 + w\left(\frac{r}{R}\right)^2}{1 + \exp\left(\frac{r-R}{a}\right)}, \tag{10}$$

and where R is the radius of the ion, a is the thickness of the skin of the nucleus and w is an additional parameter for describing nucleus which has a maximum density at $r > 0$. The parameter ρ_0 is determined by the normalization condition $\int \rho(r)\mathrm{d}^3r{=}A$, where A is the number of nucleons in the ion. For ^{208}Pb $R = (6.62 \pm 0.06)$ fm, $a = (0.546 \pm 0.010)$ fm and $w = 0$ [36]. Using this distribution nucleons are placed so that no nucleons inside the ion overlap. Nucleons are considered overlapping in the ion when the distance between two nucleons is $d < 0.4$ fm.

Impact parameter for the collision is chosen randomly from the geometrical distribution $\mathrm{d}P/\mathrm{d}b \sim b$, and b spans from 0 to a $b_{\mathrm{max}} > 2R$, where R is the radius of the ion. For ^{208}Pb the sufficiently large maximum impact parameter $b_{\mathrm{max}} \approx 20$ fm.

When b is known, two ions with transverse positions $(-b/2)$ and $(b/2)$ are created with the modified Woods-Saxon distribution of equation 10 as has been done in figure 11. When the two ions are created, there is almost always some transverse overlap between the nucleons of different ions. Nucleons in different ions are considered overlapping, when the transverse distance between the nucleons in different ions is $d_{\mathrm{T}} < \sqrt{\sigma_{\mathrm{NN}}^{\mathrm{inel}}/\pi}$, where $\sigma_{\mathrm{NN}}^{\mathrm{inel}}$ is the nucleon–nucleon inelastic cross section. The number of all nucleon–nucleon pairs that overlap is the number of collisions N_{coll}. Nucleons that overlap with at least one nucleon from the other nucleus are called participants, and if nucleon is not a participant, it is a spectator. Results from the MC Glauber simulation [36] in lead–lead collisions at $\sqrt{s_{\mathrm{NN}}}$= 2.76 TeV are collected to table 1.

2.6 PYTHIA event generator

In experimental data analysis, it is typical to start from simpler systems and progress towards the more complicated cases. In this thesis, the simplest system is a proton–proton collision. In each case, one also needs to correct for various detector effects, as there are no perfect detectors. In the jet analysis, a commonly used tool to correct for detector effects is so called unfolding method, that is described in detail in chapter 5.5. I use a MC based event generator Pythia [37], that can be used to simulate many different collision systems, and particularly proton–proton collisions. I have simulated proton–proton collisions in various collision energies in order to show that Pythia does give a fair description of the p_{T} spectra of jets formed of charged particles studied in this thesis. Hence the Pythia can be considered to provide a realistic MC truth for detector response simulations, see section 5.5 for details.

Pythia uses a random number generator to generate a hard parton-level process according to equation 4. The hard process is then supplemented with a rich phenomenology in order to obtain a description for a complete event. Initial and final state radiation describe the softer but calculable QCD radiation of the ingoing and outgoing partons. Pythia also contains a description for multi-parton interactions in a single collision event, and partons related to these processes can also branch. After the partonic evolution has finished, the hadronization is described by the Lund string model, and lastly unstable resonances are let to decay.

Pythia results are systematically compared with all available experimental data and the parameters of the program are tuned accordingly. There are several dedicated studies to tune the different event generators [38], particularly Pythia. Pythia has been shown to be excellent in describing the high energy proton–proton collisions, and as such, it can be used as a test bench for various physics analysis.

3 Jet reconstruction

3.1 Jet definition

As direct measurements on a partonic level cannot be done, one needs to define rigorously how jets can be obtained from the final state particles, and how well they represent the original hard partons. There are several ways to define a jet and these techniques have been used for decades by now. In this thesis I have used the k_T and anti-k_T jet reconstruction algorithms [39, 40] that are implemented in and provided by the FastJet [41] library, which is specialized in jet reconstruction. These algorithms define a "distance" between two particles or jets,

$$d_{ij} = d_{ji} = \min(p_{\mathrm{T},i}^{\pm 2}, p_{\mathrm{T},j}^{\pm 2}) \frac{\Delta R_{ij}^2}{R}, \tag{11}$$

where $+$ is for the k_T algorithm, $-$ for the anti-k_T algorithm, R is a resolution parameter, and $\Delta R_{ij}^2 = (\eta_i - \eta_j)^2 + (\phi_i - \phi_j)^2$, where η_i and ϕ_i refer to the pseudorapidity and azimuthal angle of particle i. For each particle or jet there is also the definition of distance to the beamline

$$d_{\mathrm{B},i} = p_{\mathrm{T},i}^{\pm 2}, \tag{12}$$

where again $+$ is for the k_T and $-$ for the anti-k_T algorithm. Using these distances the jets can be reconstructed from given particles. A characteristic feature of the k_T and anti-k_T algorithms is that each particle in an event will belong to some jet after reconstruction. First step is to declare every particle, in practise a track or a calorimeter cluster, to a so called pseudojet. Pseudojet is an object that can contain any number of particles inside. Then all distances according to equations 11 and 12 are calculated and the smallest distance is picked. If the smallest distance is between two pseudojets, they are then combined into a new, single pseudojet. If the smallest distance happens to be between a pseudojet and the beamline, that pseudojet is declared as a final jet and is left out of the rest of the calculation. This procedure is repeated until all pseudojets are declared as final jets and no pseudojets remain. Combining two pseudojets can be done in several different recombination schemes [41–43]. In this thesis, I use the so called p_T scheme, where each pseudojet is rescaled so that the energy is equal to the three-momentum size, effectively making

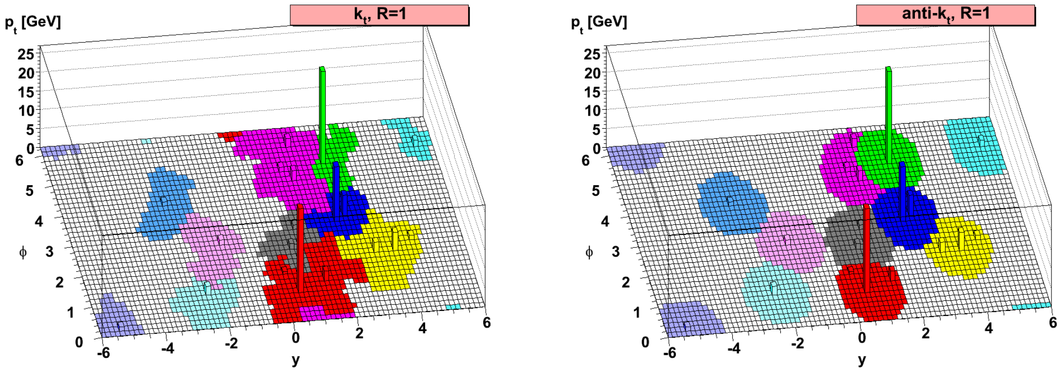

(a) k_{T} algorithm reconstructed jets. **(b)** Anti-k_{T} algorithm reconstructed jets.

Figure 12. Comparison of k_{T} and anti-k_{T} jet reconstruction algorithms in (y,ϕ) plane, where y is rapidity and ϕ the azimuthal angle. The same particle content was used in both cases. Figures are originally from publication [40].

each particle massless. Then recombination is done by

$$\begin{aligned} p_{\mathrm{T},r} &= p_{\mathrm{T},i} + p_{\mathrm{T},j} \\ \phi_r &= \frac{p_{\mathrm{T},i}\phi_i + p_{\mathrm{T},j}\phi_j}{p_{\mathrm{T},i} + p_{\mathrm{T},j}} \\ \eta_r &= \frac{p_{\mathrm{T},i}\eta_i + p_{\mathrm{T},j}\eta_j}{p_{\mathrm{T},i} + p_{\mathrm{T},j}}, \end{aligned}$$

where indices i and j refer to the pseudojets that are being combined, and the new pseudojet will have the transverse momentum $p_{\mathrm{T},r}$, azimuthal angle ϕ_r and pseudorapidity η_r.

The biggest difference between the k_{T} and anti-k_{T} algorithms is that the former starts building up the jets from small transverse momentum particles, because in equation 11 small transverse momentum pseudojets have a smaller distance. On the other hand, in equation 11 the anti-k_{T} algorithm has a negative power of the p_{T} so this time the reconstruction starts from the high transverse momentum particles, as those have a smaller distance. The comparison between these two algorithms on (y,ϕ) plane is illustrated in figure 12. The anti-k_{T} algorithm creates clear cones around the hardest particles, while the k_{T} algorithm makes unintuitive jet shapes around the same hard particles. This means that also the area of a jet can change notably between different reconstruction algorithms.

3.2 Background subtraction

A heavy ion collision can have over two thousand charged particles detected by the ALICE detector at mid rapidity. Most of the particles are soft, but still add up when reconstructing jets, so in order to recover information about the hard partons which form hard jets, the background has to be taken into account. The basic idea is to determine the background p_{T} density ρ and background mass density ρ_m for subtracting the background from jets event by event [44]. Bigger jets include more background, so also jet areas need to be calculated. There are several different ways of defining a jet area [45]. One of the most popular techniques makes use of artificial particles dubbed "ghost particles", which have infinitesimally small transverse momentum. These artificial particles are placed uniformly in the $\eta - \phi$ acceptance of the experiment, and then jets are reconstructed normally from real particles and ghosts. This does not change the set of particles which are included in jets as the k_{T} and anti-k_{T} jet finding algorithms are infrared safe. The area of a jet is then defined by the spatial region from where ghosts are clustered to the given jet.

The k_{T} algorithm is used for determining the background densities. First of all, the event is reconstructed into jets by using the k_{T} algorithm. Then each jet has

$$p_{\mathrm{T,jet}} = \sum_{i \in \mathrm{jet}} p_{\mathrm{T},i}, \tag{13}$$

$$m_{\mathrm{jet}} = \sum_{i \in \mathrm{jet}} \left(\sqrt{p_{\mathrm{T},i}^2 + m_i^2} - p_{\mathrm{T},i} \right), \tag{14}$$

where i runs over all the particles in that specific k_{T} jet. Densities can be calculated from

$$\rho = \underset{\mathrm{jets}}{\mathrm{median}} \left\{ \frac{p_{\mathrm{T,jet}}}{A_{\mathrm{jet}}} \right\} \tag{15}$$

$$\rho_m = \underset{\mathrm{jets}}{\mathrm{median}} \left\{ \frac{m_{\mathrm{jet}}}{A_{\mathrm{jet}}} \right\}, \tag{16}$$

where A_{jet} is the area of the k_{T} jet.

In order to define area-four-vector, it is convenient to write the momentum four-vector as

$$\begin{aligned} p^\mu &= (E, p_x, p_y, p_z) = \left(\sqrt{p_{\mathrm{T}}^2 + p_z^2 + m^2}, p_x, p_y, p_z \right) \\ &= p_{\mathrm{T}} \left(\sqrt{1 + \left({}^{m}/_{p_{\mathrm{T}}}\right)^2} \cosh y, \cos\phi, \sin\phi, \sqrt{1 + \left({}^{m}/_{p_{\mathrm{T}}}\right)^2} \sinh y \right) \\ &\overset{\frac{m}{p_{\mathrm{T}}} \ll 1}{\approx} p_{\mathrm{T}} \left(\cosh\eta, \cos\phi, \sin\phi, \sinh\eta \right) \\ &\equiv p_{\mathrm{T}}\, n^\mu \left(\phi, \eta\right), \end{aligned} \tag{17}$$

and then with the help of n^μ the area four-vector has been defined in the FastJet package as

$$A^\mu = \iint\limits_{A_{\mathrm{jet}}} \mathrm{d}\phi \mathrm{d}\eta \; n^\mu \left(\phi,\eta\right), \tag{18}$$

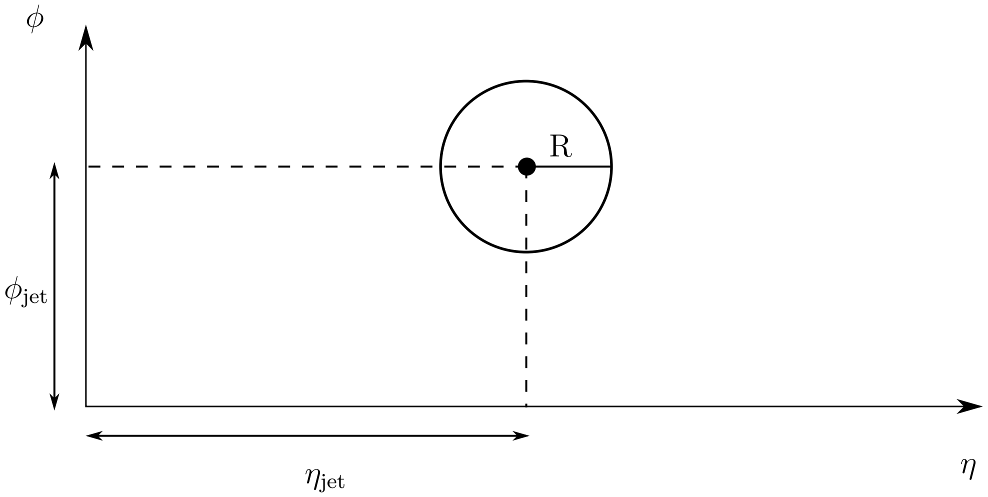

Figure 13. A jet reconstructed by the anti-k_{T} algorithm in an arbitrary position.

where the integral is over the area of the jet at hand. This area four-vector is calculated by the FastJet package. Using the area-four-vector and densities of the heavy ion collision, the background can be subtracted with

$$p^{\mu}_{\text{corr}} = p^{\mu} - \left[(\rho + \rho_m)\, A^{E}_{\text{jet}},\ \rho A^{x}_{\text{jet}},\ \rho A^{y}_{\text{jet}},\ (\rho + \rho_m)\, A^{z}_{\text{jet}} \right]. \tag{19}$$

In order to have a clearer physical image of the area four-vector, next I want to demonstrate that in the limit of small jet area the transverse component of the jet area is the geometrical area of the jet in the (η,ϕ) space. Consider now a small circular jet at a point $(\eta_{\text{jet}},\phi_{\text{jet}})$, where the jet cone radius $R \ll 1$, as depicted in figure 13. As can be seen in figure 12b, this is a reasonable approximation for the anti-k_{T} jets as they are usually circular and with relatively small $R = 0.4$.

For example the energy component for this jet can be calculated as

$$A^{E} = \iint_{A_{\text{jet}}} \mathrm{d}\phi \mathrm{d}\eta \cosh \eta. \tag{20}$$

Now presenting (η,ϕ) in cylindrical coordinates (r,θ) with a shift $(\eta_{\text{jet}},\phi_{\text{jet}})$ gives

$$\eta \to \eta + \eta_{\text{jet}} = r\cos\theta + \eta_{\text{jet}} \tag{21}$$

$$\phi \to \phi + \phi_{\text{jet}} = r\sin\theta + \phi_{\text{jet}}, \tag{22}$$

where r is the radial part and θ is the angle part in the cylindrical coordinate system.

Now the integral stands as

$$\begin{aligned}
A^E &= \int_0^{2\pi}\int_0^{R} \mathrm{d}\theta \mathrm{d}r \; r \cosh\left(r\cos\theta + \eta_{\mathrm{jet}}\right) \\
&= \int_0^{2\pi}\int_0^{R} \mathrm{d}\theta \mathrm{d}r \; r \left[\cosh\left(r\cos\theta\right)\cosh\eta_{\mathrm{jet}} + \sinh\left(r\cos\theta\right)\sinh\eta_{\mathrm{jet}}\right] \\
&\overset{R\ll 1}{\simeq} \int_0^{2\pi}\int_0^{R} \mathrm{d}\theta \mathrm{d}r \; r \left[\cosh\eta_{\mathrm{jet}} + r\cos\theta\sinh\eta_{\mathrm{jet}}\right] \\
&= \cosh\eta_{\mathrm{jet}} \int_0^{2\pi}\mathrm{d}\theta \int_0^{R}\mathrm{d}r \; r + \sinh\eta_{\mathrm{jet}} \underbrace{\int_0^{2\pi}\mathrm{d}\theta\cos\theta}_{=0} \int_0^{R}\mathrm{d}r \; r^2 \\
&= \pi R^2 \cosh\eta_{\mathrm{jet}} = A_{\mathrm{jet}}\cosh\eta_{\mathrm{jet}}. \qquad (23)
\end{aligned}$$

The other components are calculated in a similar fashion. The area four-vector for a certain jet with circular area, with small R and massless constituents can be written as

$$\begin{aligned}
A^\mu &\approx A_{\mathrm{jet}}\left(\cosh\eta_{\mathrm{jet}}, \cos\phi_{\mathrm{jet}}, \sin\phi_{\mathrm{jet}}, \sinh\eta_{\mathrm{jet}}\right) \qquad (24)\\
&= A_{\mathrm{jet}}\; n^\mu\left(\phi_{\mathrm{jet}}, \eta_{\mathrm{jet}}\right). \qquad (25)
\end{aligned}$$

Now it is easy to see that the transverse area is approximately the area itself

$$A_{\mathrm{T}} = \sqrt{A_x^2 + A_y^2} \approx \sqrt{A_{\mathrm{jet}}^2\cos^2\phi_{\mathrm{jet}} + A_{\mathrm{jet}}^2\sin^2\phi_{\mathrm{jet}}} = A_{\mathrm{jet}}. \qquad (26)$$

Using this information and equation 19 it is now quite clear to see that for transverse momentum the background subtraction is simply

$$p_{\mathrm{T,corr}} = p_{\mathrm{T}} - \rho A_{\mathrm{jet}}. \qquad (27)$$

The effect of the background subtraction is demonstrated with a simple Pythia study. A hard event is forced to have approximately 80 GeV jet in every event. This hard event is embedded into 1200 minimum bias Pythia events, which corresponds roughly to a heavy ion collision in the 5–10 % centrality range according to table 1. in figure 14 the effect of background removal can be seen. In red there is jet transverse momentum spectrum from the hard event and in black the heavy ion collision with the embedded hard event, and then the background is subtracted. It is clearly seen in this simple example that the background removal works, but has an effect on the original spectrum, which has to be taken into account.

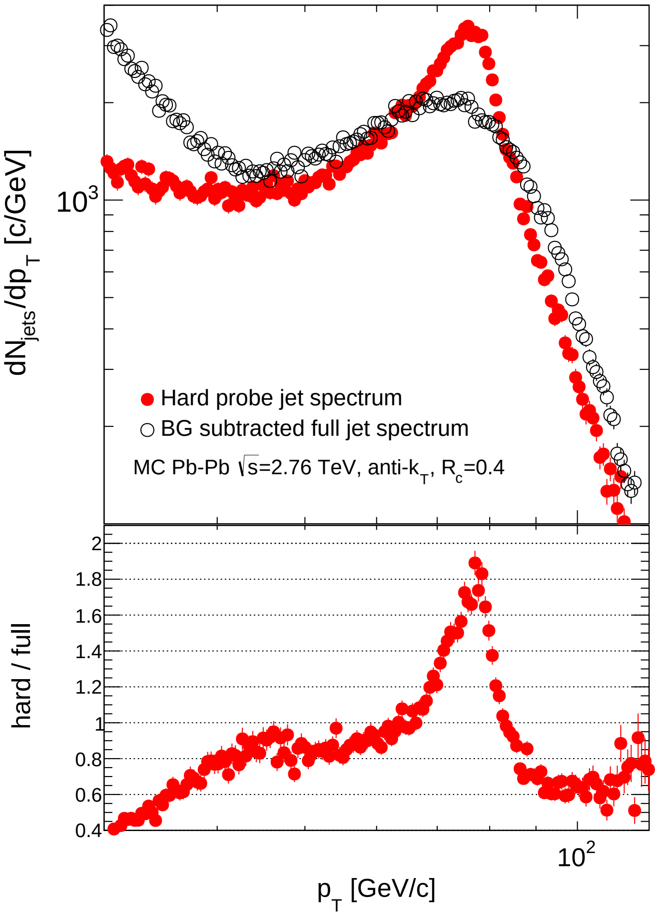

Figure 14. In the top panel filled red circles show hard full jet spectrum with 79.5 GeV $< p_{\mathrm{T,hard}} <$ 80.5 GeV and black open circles show the spectrum with hard event embedded in a heavy ion environment and background subtracted. Lower panel shows the ratio between the two. This figure serves as an example of the effects that background subtraction has for a jet spectrum. Note that in this thesis I have used solely charged jets, but this figure shows the full jet spectrum.

4 Experimental setup

4.1 A Large Ion Collider Experiment

One of the experiments focusing on studying the QGP through ultrarelativistic heavy ion collisions is A Large Ion Collider Experiment (ALICE) at the LHC at CERN. The LHC hosts several collaborations and biggest of them are CMS, ATLAS, LHCb and ALICE, see figure 15a. The bigger the accelerator is, more energy is needed when injecting a beam, and because of that, the LHC needs several boosters in order to work. The initial acceleration of the particles is done by a linear accelerator, after which comes a series of circular boosters. From the linear accelerator, particles are first injected into the Proton Synchrotron Booster (PSB), then into the Proton Synchrotron (PS), the Super Proton Synchrotron (SPS) and finally into the LHC.

In figure 15b the subdetectors of the ALICE experiment are presented. It has several forward and barrel subdetectors and I will explain the main motivation for them with emphasis on detectors which are important for this thesis. The most important detectors for this thesis are the V0 and TPC detectors. V0 consists of two arrays of scintillator counters, V0A, which is located 340 cm from the collision vertex at the range $2.8 < \eta < 5.1$, and V0C is located only 90 cm from the vertex at the range $-3.7 < \eta < 1.7$ [47]. V0 is used as a minimum bias trigger V0AND, which requires a hit in both V0A and V0C. These have been estimated to have approximately 83 % efficiency for non-single diffractive proton–proton collisions [48], over 99 % efficiency for proton–lead collisions [49] and 100 % for lead–lead collisions, except for the very peripheral collisions [48], which are not discussed or used in this work.

Other duty of the V0 detector is to measure the centrality classes. Heavy ion collisions are categorized into centrality classes using the sum of amplitudes in the detectors V0A and V0C. The corresponding centrality classes for the summed V0 amplitudes are calculated with the help of negative binomial distribution fit [36], which is presented in figure 16. The fit has three parameters and the fit values can be seen in the figure. To calculate the centrality classes the distribution is integrated in parts in a similar way as in chapter 2.5.

Innermost detectors are the Inner Tracking System (ITS) pixel, drift and strip detectors and the Time Projection Chamber (TPC), that all detect charged particles, and lastly the Transition Radiation Detector (TRD) which on the other hand is for electron detection. The Time Of Flight (TOF) detector is used for particle identification in the intermediate momentum range, up to 2.5 GeV for pions and kaons and up to 4 GeV for protons. The High-Momentum Particle Identification Detector (HMPID) is used to further extend the particle identification range, up to 3 GeV for pions and kaons and up to 5 GeV for protons. The Electromagnetic Calorimeter (EMCal) is important for detecting photons and electrons, but it consists of only a third of the total azimuthal angle. ALICE also has Zero Degree Calorimeters (ZDC) which are located about 115 meters away from the detector on both directions. The ZDC can detect the spectator nucleons in heavy ion or proton–lead collisions. This measurement can be used as an alternative estimate for the centrality to the V0 sum measurement.

ALICE has a solenoidal magnet which operates at 0.5 T. When comparing to the CMS experiment magnet which is 4 T [50], the ALICE magnet seems weak. The reason for a weaker magnetic field in ALICE is that it provides a quite good middle ground for the detector as the transverse momentum resolution remains good down to as low values as 0.1 GeV, and up to values at most 100 GeV. A low momentum resolution is important for ALICE as for example precise multiplicity measurements with particle identification are essential in many physics programs in heavy ion collisions.

The TPC detector is a cylindrical detector that covers the whole azimuthal angle and $|\eta| < 0.9$ [47]. The cylinder extends radially from 85 cm till 247 cm, and is located at -250 cm $< z <$ 250 cm. It tracks down charged particle trajectories and handles particle momentum and identification with the use of magnetic field, electric potential inside and tracking gas inside. The gas of the detector was a mixture of neon (85.7 %), carbon-dioxide (9.5 %) and dinitrogen (4.8 %) until the end of 2010. From 2011 on it has been filled only with neon (90 %) and carbon-dioxide (10 %) [49].

4.2 Data and Monte Carlo production

In this work, I have used several MC simulations, namely stand alone and full simulations. The Pythia software is freely available on their home page [51], and in this thesis I use the term “stand alone” for Pythia studies where I generated the events with a local Linux cluster in Jyväskylä. On the other hand, “full simulations” refer to the ALICE Pythia results that have been produced by ALICE according to the ALICE standards. Compared to stand alone production, full simulations take into account more details, like for example the collision vertex distribution. ALICE MC production is also propagated through the detector using Geometry And Tracking (GEANT) simulations [52], and then the detector response is carried through the tracking and trigger algorithms. This way realistic response of the detector, tracking and triggering for a given set of particles can be achieved, and used for calculating various detector efficiency corrections. In this thesis I have used full simulations to create response matrices for correcting detector effects, which will be discussed in more detail in chapter 5.5.

The proton–proton MC events were produced mainly by a stand alone PYTHIA version 8226, otherwise the version is mentioned. As for the data results, I have studied the ALICE proton–lead data which was recorded in 2013 and the results for lead–lead are from 2015. There were approximately 100 million events total in proton–lead collisions and approximately 55 million lead–lead events for the heavy ion results.

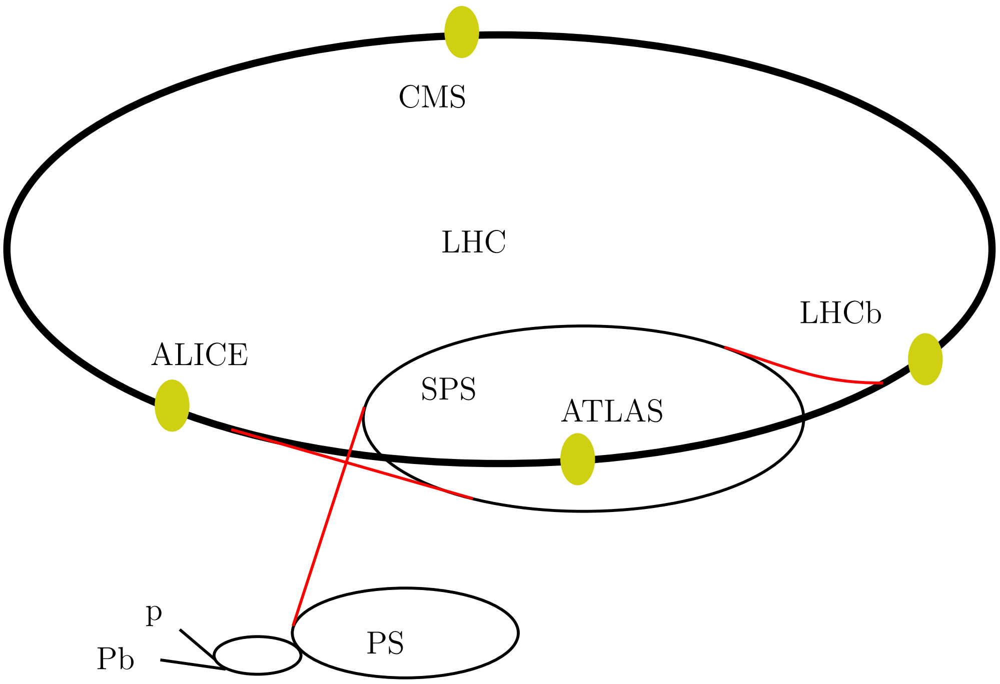

(a) A schematic picture of the LHC apparatus and the several boosters located at CERN. Four biggest experiments, CMS, ATLAS, LHCb and ALICE, are marked on the LHC. Figure source [46].

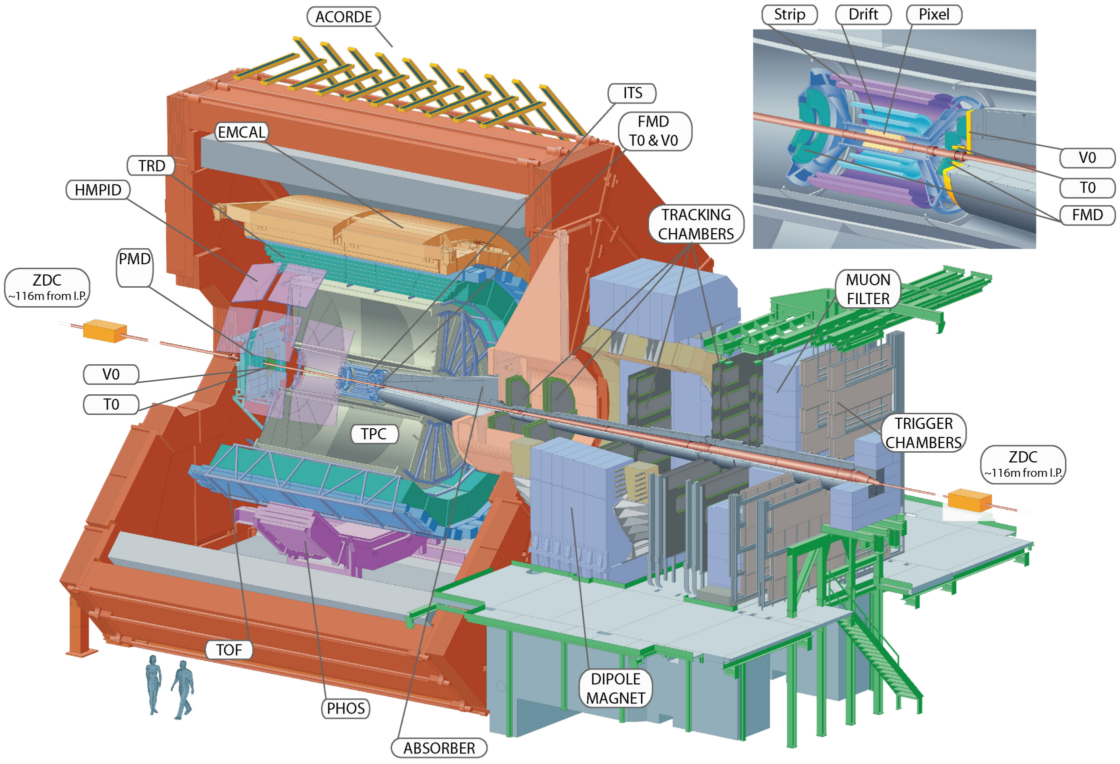

(b) The ALICE detector with subdetectors marked.

Figure 15. The experimental setup at the LHC and ALICE there.

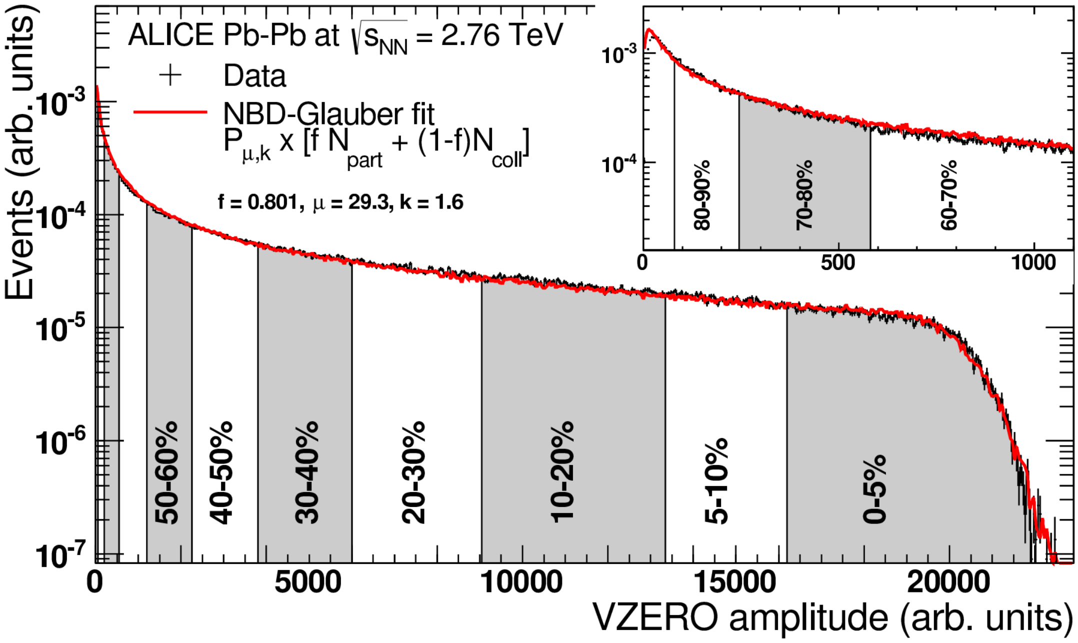

Figure 16. Distribution of the sum of amplitudes in the V0A and V0C detectors in ALICE [36], categorized into centrality classes.

5 Analysis

5.1 Dijets

In this work, the momentum of a dijet is defined to be the leading jet four-momentum summed with subleading jet four-momentum, $p_{\mathrm{jj}} = p_1 + p_2$. This kind of a system has certain kinematical restrictions which will be discussed in the following text.

Particles are called to be on-shell, if

$$p^2 = m^2,$$

when using the metric tensor $g_{\mu\nu} = \mathrm{diag}\{1, -1, -1, -1\}$, where m is the mass of the particle. Due to imperfect particle identification it is also common to set the masses of the dijet constituents to zero, or alternatively to pion mass. In this thesis, the p_{T} recombination scheme of the jet algorithm sets all constituents massless.

Let us start from a simple electron–positron scattering $e^+ + e^- \rightarrow \gamma^* \rightarrow q + \bar{q}$ at the center-of-mass frame of the scattering. Momentum conservation requires that the outgoing quarks have to be back-to-back with equal momenta, $\vec{p}_{\bar{q}} = -\vec{p}_q$. Hence the invariant mass of the dijet system becomes

$$\begin{aligned} M_{\mathrm{jj}}^2 &= (p_q + p_{\bar{q}})^2 = m_q^2 + m_{\bar{q}}^2 + 2\left(E_q E_{\bar{q}} - \vec{p}_q \cdot \vec{p}_{\bar{q}}\right) \\ &\approx 0 + 0 + 2\left|\vec{p}\right|^2 (1 - \cos\pi) = 4\left|\vec{p}\right|^2 \end{aligned}$$

where $|\vec{p}| \equiv |\vec{p}_q| = |\vec{p}_{\bar{q}}|$. In above we have approximated that the quarks are massless. Thus, in the ideal electron-positron scattering to quark and anti-quark, the invariant mass of the dijet system is simple in mid-rapidity

$$M_{\mathrm{jj}} \approx 2p_{\mathrm{T}}. \tag{28}$$

In proton–proton collisions, the kinematics become slightly more complicated because partons entering to the hard scattering have different incoming momenta in the longitudinal direction. Let us consider a scattering $a + b \rightarrow c + d$ for massless partons. For incoming partons

$$\begin{aligned} p_a^\mu &= \frac{\sqrt{s}}{2}(x_a,0,0,x_a) \\ p_b^\mu &= \frac{\sqrt{s}}{2}(x_b,0,0,-x_b), \end{aligned}$$

where $0 < x < 1$ is the momentum fraction that a parton has from the momenta of the incoming proton, dictated by the parton distribution functions (as in equation 2). Typically $x_a \neq x_b$ and hence the longitudinal momenta of the incoming partons are not equal in magnitude. This means that the center-of-mass frame of the incoming protons is not the center-of-mass frame of the hard scattering. However, since there is no initial transverse momentum in the collision, the outgoing momenta for massless partons can be written explicitly by using p_T and pseudorapidity η

$$\begin{aligned} p_c^\mu &= p_\mathrm{T} \left(\cosh \eta_c, \cos \phi, \sin \phi, \sinh \eta_c\right) \\ p_d^\mu &= p_\mathrm{T} \left(\cosh \eta_d, -\cos \phi, -\sin \phi, \sinh \eta_d\right). \end{aligned}$$

Momentum conservation $p_a + p_b = p_c + p_d$ gives relations and restrictions to the transverse momentum, rapidity and momentum fractions, like

$$x_{a,b} = \frac{p_\mathrm{T}}{\sqrt{s}} \left(e^{\pm\eta_c} + e^{\pm\eta_d}\right).$$

The dijet mass in proton–proton collisions becomes

$$\begin{aligned} M_\mathrm{jj}^2 &= (p_c + p_d)^2 \\ &= 2p_\mathrm{T}^2 \left(\cosh \eta_c \cosh \eta_d - \sinh \eta_c \sinh \eta_d + \cos^2 \phi + \sin^2 \phi\right) \\ &= 2p_\mathrm{T}^2 \left(1 + \cosh \Delta\eta\right), \end{aligned} \tag{29}$$

where $\Delta\eta = \eta_c - \eta_d$. This result is reduced to equation 28 for the mid-rapidity electron–positron scattering since in that case the $\Delta\eta = 0$.

In this thesis I study general dijet systems, for which these ideal results are not exact. Especially in heavy ion collisions there is a clear imbalance between transverse momenta of the dijet partners already due to the energy loss and also from next-leading-order perturbative QCD effects. Generally the outgoing jet momenta can be written in terms of rapidity

$$\begin{aligned} p_c^\mu &= \left(m_\mathrm{T,c} \cosh y_c, p_{\mathrm{T},c} \cos \phi_c, p_{\mathrm{T},c} \sin \phi_c, m_\mathrm{T,c} \sinh y_c\right) \\ p_d^\mu &= \left(m_\mathrm{T,d} \cosh y_d, p_{\mathrm{T},d} \cos \phi_d, p_{\mathrm{T},d} \sin \phi_d, m_\mathrm{T,d} \sinh y_d\right), \end{aligned}$$

and with these, the dijet mass in a general system can be achieved similarly as before

$$\begin{aligned} M_\mathrm{jj}^2 &= m_c^2 + m_d^2 + 2\left(m_\mathrm{T,c} m_\mathrm{T,d} \cosh \Delta y - p_{\mathrm{T},c} p_{\mathrm{T},d} \cos \Delta\phi\right) \\ &\approx 2 p_{\mathrm{T},c} p_{\mathrm{T},d} \left(\cosh \Delta\eta - \cos \Delta\phi\right), \end{aligned} \tag{30}$$

where $m_\mathrm{T}^2 = p_\mathrm{T}^2 + m^2$ is transverse mass, m is the single-jet invariant mass, and $\Delta\phi = \phi_c - \phi_d$. The approximation holds for massless jets. Also this result reduces to the ideal case when transverse momentums are set equal and $\Delta\phi = \pi$. In this thesis, I will take the jet four-momenta as given by FastJet packet using the p_T scheme and calculate the exact four-vector scalar products from them.

5.2 Event and track selection

In this thesis, I have based my studies solely on charged particles. ALICE has limited ways to detect neutral particles, as ALICE does not have a hadronic calorimeter. Photons and electrons can be studied with EMCal, but EMCal has a limited azimuthal acceptance, which is detrimental for a dijet analysis as the jets are expected to be back-to-back. The dijet calorimeter DCAL became operational in the beginning of run 2 in 2015. However, the challenge is that DCAL has been build around the fine granularity calorimeter PHOS that makes the calibration very challenging, if one would like to use the combined DCAL+PHOS clusters in the dijet analysis. No serious attempt to that direction had been done in ALICE at the time when this thesis was prepared. Thus, the acceptance restrictions for neutral particles alone give a good reason to search only charged particles, as ALICE TPC has a full azimuthal angle acceptance for charged particles. Jets reconstructed by using only charged particles as an input are called charged jets, and this term is used widely in this thesis.

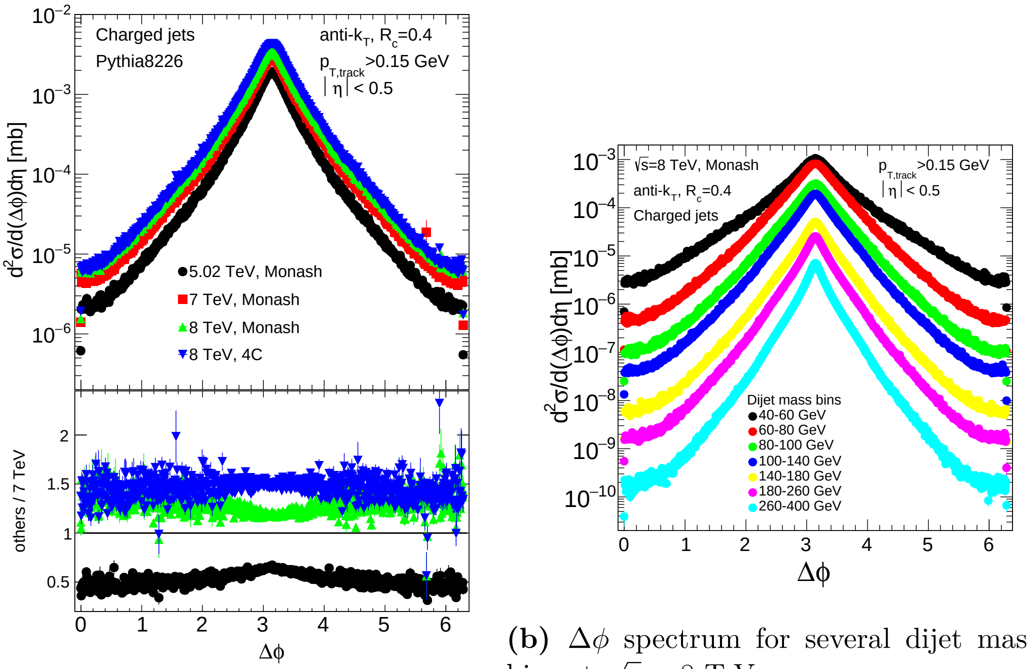

(a) Top panel shows a comparison of $\Delta\phi$ distributions at various $\sqrt{s}$. Bottom panel shows a ratio plot of each spectrum divided by 7 TeV results.

(b) $\Delta\phi$ spectrum for several dijet mass bins at $\sqrt{s} = 8$ TeV.

Figure 17. $\Delta\phi$ spectra of the dijet system in proton–proton MC collisions, where $\Delta\phi$ is the azimuthal angle between the two jets in the dijet system. The dijet leading jet and subleading jet are required to have $p_{\mathrm{T}} > 20$ GeV.

In my dijet analysis, I have required track transverse momentum to be over 0.15 GeV, because tracking errors grow large below that limit in ALICE. Jet pseudorapidity acceptance is always $|\eta| < 0.8 - R$ or less, where R is the jet resolution parameter. The TPC acceptance for tracks is $|\eta| < 0.9$, and a safe cut without effects caused by the very edge of TPC is $|\eta| < 0.8$, so in order to acquire only jets which are fully inside the safe TPC acceptance, the jet acceptance has to be $|\eta| < 0.8 - R$ or less. Single jets with $p_{\mathrm{T}} < 5$ GeV are discarded, as well as jets with smaller area than $0.6\pi R^2$. If a jet leading constituent has a transverse momentum fraction of over 0.98 compared to the jet momentum, it is discarded as well. Both jets of each dijet are required to have over 20 GeV transverse momentum in order to leave out dijets which are not formed from a hard parton–parton interaction. For the lead–lead results a jet constituent cut was used. The cut requires that each jet should have the leading constituent $p_{\mathrm{T}} > 5$ GeV. The reason for this cut is to reduce combinatorial jets, which are made only of soft particles.

In addition, I have used a dijet $\Delta\phi$ cut. If the two jets have an azimuthal angle between them in the range of $\Delta\phi \in [0,2\pi[$, then only dijets with

$$|\Delta\phi - \pi| < \frac{\pi}{2}$$

are selected, in order to retain the geometrical intuition that dijets should be approximately back-to-back. Dijets which are on the same hemisphere are mainly formed from splitted or combinatorial jets, which are not relevant for this thesis. Or, it can happen that a hard dijet is formed in the event, but either of the dijet partners lands out of the detector acceptance. Then the leading jet splits by a chance which creates a dijet with a small $\Delta\phi$. The $\Delta\phi$ spectra of different MC runs are drawn in figure 17a. Figure 17b shows the $\Delta\phi$ distributions in several different dijet mass bins. The distributions get narrower with higher dijet masses, which is to be expected.

5.3 Double differential cross section

In order to measure the cross section for a given process, we need to know how big a fraction of inelastic cross section σ_{inel} is seen by the minimum bias trigger used to collect the data. This is called the visible cross section of the collision $\sigma_{\mathrm{V0AND}} = \varepsilon\sigma_{\mathrm{inel}}$, where ε is the fraction of inelastic events which are triggered. The visible cross section can be measured using a process called van der Meer scan [53]. The details for this process and results are found in [54] for proton–proton and in [55] for proton–lead collisions. Following [55], the process goes as follows: Measuring the rate of collisions R as the function of the beam separation Δx and Δy allows to calculate the luminosity of the head on collisions of two particle bunches with particle intensities N_1 and N_2. The luminosity is

$$L = \frac{N_1 N_2 f_{\mathrm{rev}}}{h_x h_y}, \tag{31}$$

where f_{rev} is the frequency of particle bunches crossing and h_x and h_y are the effective beam widths in horizontal and vertical directions. The transverse widths h_x and h_y can be calculated by integrating the rate in the function of the separation Δx and Δy respectively. In practice the beams are scanned in x and y directions, measuring the rate of events which can be seen in detectors V0A and V0C simultaneously. Then the visible cross section is achieved as

$$\sigma_{\mathrm{V0AND}} = \frac{R(0{,}0)}{L}, \tag{32}$$

where $R(0{,}0)$ refers to the rate of events in head-on collisions using the ALICE minimum bias trigger V0AND.

When the visible cross section is known, the double differential jet cross section is

$$\frac{\mathrm{d}^2\sigma}{\mathrm{d}p_{\mathrm{T}}\mathrm{d}\eta} = \frac{1}{\mathcal{L}_{\mathrm{int}}}\frac{\Delta N}{\Delta p_{\mathrm{T}}\Delta\eta} = \frac{\epsilon_{\mathrm{vtx}}\sigma_{\mathrm{V0AND}}}{N_{\mathrm{events}}}\frac{\Delta N}{\Delta p_{\mathrm{T}}\Delta\eta}, \tag{33}$$

where $\mathcal{L}_{\mathrm{int}}$ is the integrated luminosity, ϵ_{vtx} is vertex reconstruction efficiency, and N_{events} is the total number of events collected with minimum bias trigger V0AND, ΔN number of jets in a certain p_{T} bin of the width Δp_{T} and in the pseudorapidity acceptance $\Delta\eta$.

The vertex is usually calculated with the use of tracks in the TPC and in ITS, but if that fails, SPD can be used for vertex positioning. Still in about 10 % of the events a vertex cannot be found at all [54], and this is corrected by setting a vertex for the event randomly using the measured vertex distribution. The inefficiency of the vertex reconstruction as a whole is fixed by correcting the spectrum by ϵ_{vtx}. For proton–lead V0AND minimum bias trigger $\epsilon_{\mathrm{vtx}} = 0.983$ [27].

Similarly the double differential dijet mass cross section can be achieved by using the dijet mass M_{jj} instead of the jet transverse momentum

$$\frac{\mathrm{d}^2\sigma}{\mathrm{d}M_{\mathrm{jj}}\mathrm{d}\eta} = \frac{1}{\mathcal{L}_{\mathrm{int}}}\frac{\Delta N}{\Delta M_{\mathrm{jj}}\Delta\eta} = \frac{\epsilon_{\mathrm{vtx}}\sigma_{\mathrm{V0AND}}}{N_{\mathrm{events}}}\frac{\Delta N}{\Delta M_{\mathrm{jj}}\Delta\eta}, \tag{34}$$

which is identical to equation 33, except for the dijet mass instead of jet p_{T}.

5.4 Scaling p–p cross section down for $\sqrt{s} = 5.02$ TeV results

In this work, the proton–proton data of center-of-mass energies $\sqrt{s} = 7$ TeV and $\sqrt{s} = 8$ TeV is used as a reference for MC simulations. The $\sqrt{s} = 5.02$ TeV proton–proton data has not been used as it is not yet fully calibrated. Because of this, I will compare the $\sqrt{s} = 5.02$ TeV MC results with the reference data that is scaled from the $\sqrt{s} = 7$ TeV proton–proton measurement with scaling factors obtained from MC simulations. The simulation of hard processes is done using the next-to-leading order generator POWHEG [56–58] after which the parton shower evolution and hadronization is described by PYTHIA8 [37]. For each $p_{\mathrm{T,jet}}$ bin POWHEG+PYTHIA8 is used to calculate yields for the two energies and the scaling factor is determined by

$$F(p_{\mathrm{T,jet}}) = \frac{\mathrm{yield}(p_{\mathrm{T,jet}})|^{5.02\ \mathrm{TeV,boosted}}_{\mathrm{pp,NLO}}}{\mathrm{yield}(p_{\mathrm{T,jet}})|^{7\ \mathrm{TeV}}_{\mathrm{pp,NLO}}}, \tag{35}$$

where the 5.02 TeV proton–proton collision has been boosted by $y_{\mathrm{NN}} = 0.465$ to achieve the same reference frame as the same energy proton–lead collision. This scaling factor is used p_{T} bin-by-bin to correct the spectrum. [59]

5.5 Unfolding procedure

Detector inefficiencies have to be taken into account in the data analysis. Generally some particles are lost as detectors sometimes miss particles, and this affects the measured spectra. For this kind of detector effect correction there is a technique called unfolding [60, 61]. In the unfolding method a Monte Carlo event generator, like PYTHIA, is used to generate collision events. The MC particles are all available for the user to reconstruct jets and dijets, and to measure spectra. These results are in a sense ideal, as all the particles of the collision are used. The detector response for the ideal particles is then simulated using GEANT3 [52]. This means that some of the information from the particle set is lost or distorted by some small amount. By comparing these detector results and ideal results, a response matrix can be formed. By using this information a relation can be written

$$h_{\mathrm{det}} = R h_{\mathrm{ideal}}, \tag{36}$$

where h_{det} is the detector particle histogram, R is the response matrix, and h_{ideal} is the ideal particle histogram. The response matrix that I have obtained for unfolding the proton–lead results can be seen in figure 18. The red line in these figures represents a perfect detector, where no inefficiencies would occur. Both of the response matrixes are spread out, but well concentrated around the red line. It is good to note that as the color plot also is logarithmic, the figure really is concentrated on the center line.

The challenge is that this formula needs to be reversed so that h_{ideal} can be calculated from h_{det}. For a computer, inverting a matrix is not a problem, but unfortunately finite statistics causes huge unphysical numerical oscillations in the final result. This renders the results completely useless. Fortunately several ways to invert the matrix without causing big oscillations have been developed, and in this thesis I have used the Singular Value Decomposition (SVD) method [62] and the Bayesian method [60], both implemented in the ROOUNFOLD framework [63]. Usually an unfolding method has a regularization parameter which can be used to tune the unfolding. These parameters are different for each method.

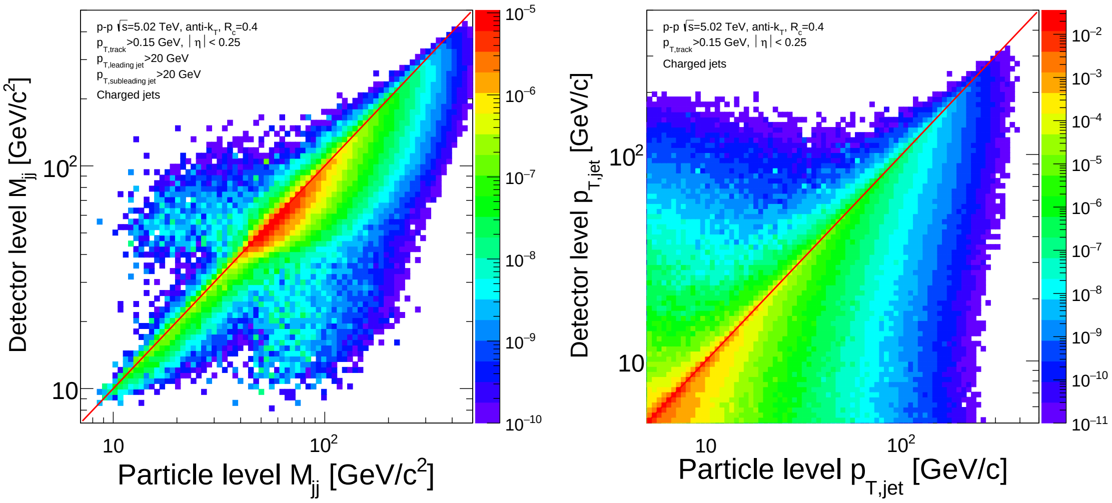

(a) Response matrix for dijet mass. **(b)** Response matrix for jet p_{T}.

Figure 18. Response matrices are created by using Monte Carlo simulations. Particles without detector effects are the particles which are received from the Monte Carlo event generator. Detector effects are simulated using the GEANT detector simulation to the particles from the MC event generator. These particle level and detector level results are compared to create these response matrices.

The general idea in the Bayesian method is to iteratively invert the response matrix. The starting point is the non-inverted matrix and each iteration is asymptotically closer to the inverted matrix, which has the huge numerical fluctuations. The goal is to find the optimal amount of iterations so that the matrix does the inverting, but not too much so that the fluctuations stay small enough. For this method the regularization parameter is the number of iterations executed.

While in Bayesian method the results are achieved by iterating, the SVD method sets conditions for the results. Generally a good condition is to require some amount of smoothness. Parts of the response matrix have dependencies which are $\propto {}^{1}\!/_{x_i}$, x_i being some histogram value of bin i. This is problematic for small values of x_i as the result grows really fast. These small x_i are normal because of the finite statistics. The regularization parameter τ introduces a damping here so that the dependency changes to be $\propto {}^{x_i}\!/_{(x_i^2+\tau)}$, so that even in small x_i the values the result will not grow too fast.

In figure 19 the ALICE proton–proton detector MC results has been unfolded with the SVD unfolding and Bayesian unfolding, with several different regularization parameters. The ratios have been done with regards to the regularization parameter seven, which was the first parameter where there was no significant change compared to the next one. The final results were unfolded with the SVD unfolding because it seemed to converge better than the Bayesian, however, both of these are necessary in the later analysis when systematic errors are calculated.

Heavy ion high-multiplicity environment introduces more complications. It was noticed in a lead–lead study by ALICE that the high p_{T} region detector response is dominated by detector effects, and the background fluctuations dominate the low p_{T} region of the spectrum [31]. Background fluctuations can indeed have a significant effect, and it affects the results even after the background subtraction described in section 3.2. To tackle this, a simulation is needed where Monte Carlo jets are embedded to heavy ion collisions, and the response matrix is then calculated after background subtraction for reconstructed jets that are matched with the embedded jets. This study has not yet been done in this analysis, and it is one of the major works ahead for obtaining the dijet result in heavy ion collisions.

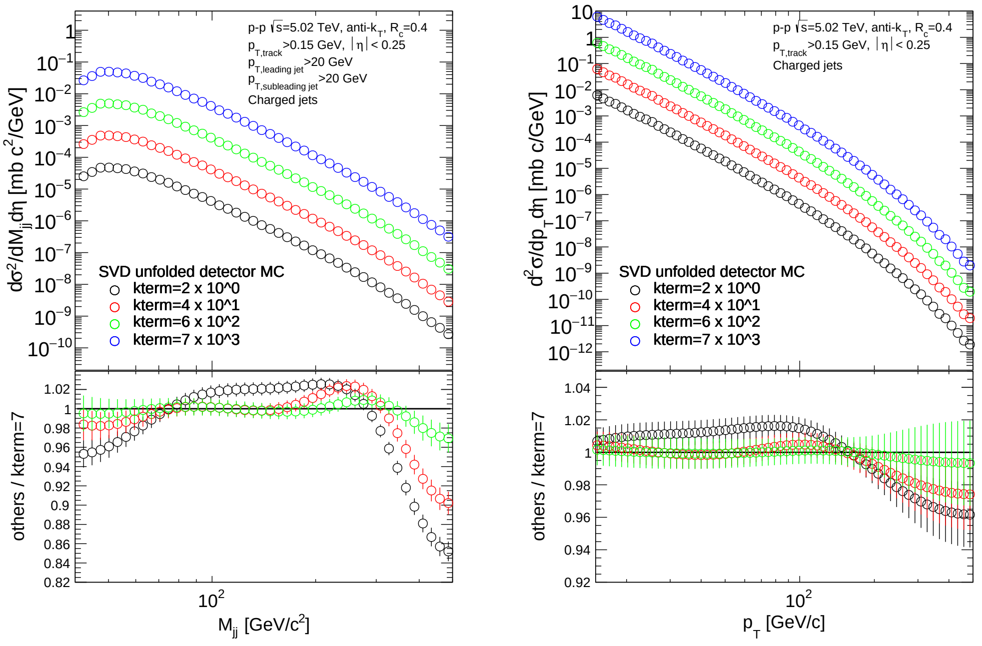

(a) Charged dijet cross section comparison for SVD unfolding.

(b) Charged jet cross section comparison for SVD unfolding.

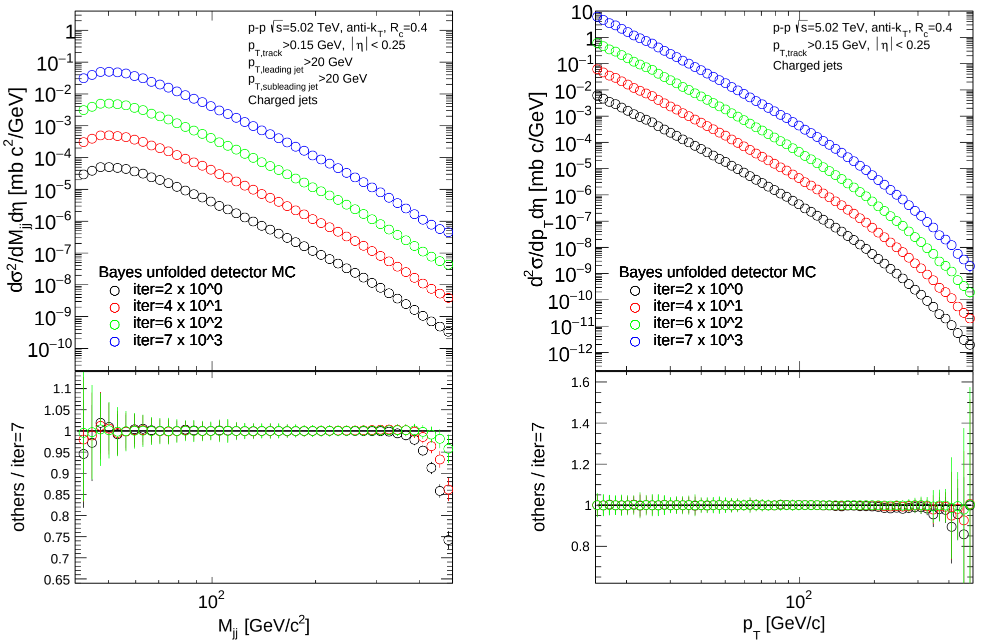

(c) Charged dijet cross section comparison for Bayesian unfolding.

(d) Charged jet cross section comparison for Bayesian unfolding.

Figure 19. Top panels show a comparison of the results with different unfolding regularization parameters. The curves have been artificially separated by multiplication factors of powers of 10 for clarity. Bottom panels show ratio plots where all cross sections have been divided by the cross section of the regularization parameter 7.

6 Results

6.1 Proton–proton collisions

Using PYTHIA8226 with tune Monash [64], I achieved MC event generator results for 8 TeV, 7 TeV and 5.02 TeV center of mass energies, by running with several different $p_{\mathrm{T,hard}}$ bins and in the end combining then. This procedure is described in appendix A. The histograms and comparison to ALICE data [27, 38] and unpublished ALICE data [65] are drawn in figure 20. PYTHIA agrees fairly well with ALICE data. The low p_{T} difference is quite large, but this has been seen also previously in [38] for especially the PYTHIA AMBT1 and PYTHIA Perugia-0 tunes. The 5.02 TeV data was scaled down from the 7 TeV data using the scaling method described in chapter 5.4. PYTHIA was ran stand alone in tune Monash, but a comparison between the tunes Monash and 4C is presented in appendix A, showing also significant differences between different PYTHIA tunes.

In figure 21 the $\Delta\phi$ cut dijet mass spectrum from stand alone PYTHIA comes really close to replicating the unpublished ALICE data when mass is over 60 GeV. The mass region below 60 GeV is, in a matter of fact, affected by the choice that leading and subleading jets are required to have over 20 GeV transverse momentum in order to be accepted as a dijet. Looking at equation 28 the 20 GeV restriction will create a deficit of dijets in the region under 40 GeV and most probably this affects at even higher masses.

6.2 Proton–lead collisions

In figures 22a and 22b a closure test of the unfolding is done. This means comparing the unfolding of the detector MC spectrum to the true MC results. The unfolded detector MC matches the true MC spectrum at dijet masses over 80 GeV, and jet p_{T} over 25 GeV but under 70 GeV. The results of the data unfolding, for both the dijet mass and jet p_{T} spectra are drawn in figures 23a and 23b. The unfolding has a uniform effect on the spectra, not depending on dijet mass or jet p_{T}. These results are compared to the ideal proton–proton MC reference in figure 24. The nuclear modification factor $R_{\mathrm{pA}}^{\mathrm{PYTHIA}}$ was calculated in the same way as in equation 1, where the number of average binary collisions in proton–lead minimum bias collisions is $\langle N_{\mathrm{coll}} \rangle = 6.9$ [27]. As the compared proton–proton spectrum was a MC production, these results should be interpreted cautiously. As has been shown in previous studies, and in appendix A, the MC spectrum can change even up to 50 % depending on the

MC generator and its tune [38]. In the jet nuclear modification factor figure, also results from an ALICE study are presented [59]. As is clearly seen, the results in the jet nuclear modification factor differ by a small margin. If this would be taken into account in the dijet nuclear modification factor, it would most probably also be close to unity, making the nuclear modification of the dijet system in proton–lead collisions minimal.

6.3 Lead–lead collisions

The lead–lead results presented in this work serve primarily as an outlook of what will be done in the near future. The background subtraction was done using equation 19. The result of background subtraction on jets in $\sqrt{s_{\mathrm{NN}}} = 5.02$ TeV lead–lead collisions can be seen in figure 25a, which serves as a demonstration of how huge the background in a heavy ion collision is even for hard jets. In the subtraction process, part of the jets are lost, and this effect was seen in figure 14. Reading from the figure, even up to 90 % correction is needed near the peak to get the original amount of jets. Also the peak seems to have shifted little bit to the lower p_{T}, but that might well be because of the low p_{T} combinatorial jets from the heavy ion background. Some of the combinatorial jets can be reduced by requiring jets to have a leading constituent particle with some lower p_{T} bound. For example in ALICE lead–lead study the leading constituent $p_{\mathrm{T}} > 5$ GeV and $p_{\mathrm{T}} > 10$ GeV restrictions were studied [31]. In both cases most of the low p_{T} jets were removed and jets above 50 GeV were left unmodified. The bigger the jet cone size, the later the cut affects.

Raw dijet mass spectra from different centrality classes have been compared to the raw proton–lead results in figure 25b. It is a fair comparison as the unfolding procedure in figure 23 was shown to have approximately a constant effect for both the dijet mass and jet p_{T} spectra. In this figure a slight excess of dijet mass is seen in 60 GeV $< M_{\mathrm{jj}} <$ 80 GeV, and a deficit in $M_{\mathrm{jj}} >$ 100 GeV. An ordering of the centrality classes is also seen in $M_{\mathrm{jj}} <$ 90 GeV, where the most peripheral class is closest to unity when compared to the proton–lead results. It is good to keep in mind that this figure presents the probability distributions, and not cross sections. Also there are multiple corrections and error sources ignored, which are discussed in the section 7.

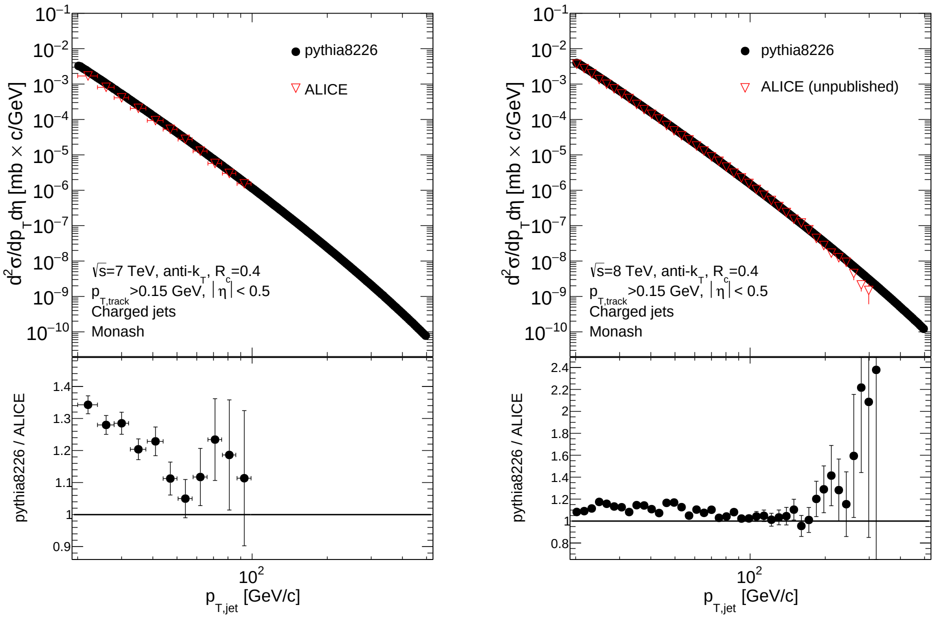

(a) $\sqrt{s}$ = 7 TeV, ALICE data from publication [38].

(b) $\sqrt{s}$ = 8 TeV, where the ALICE data are from unpublished work [65].

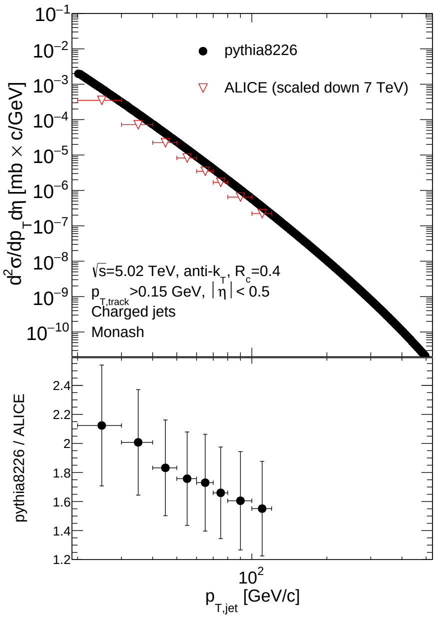

(c) $\sqrt{s}$ = 5.02 TeV. Note that ALICE data, which are from publication [27], has been scaled down from 7 TeV using 35.

Figure 20. Top panels show a comparison of charged jet cross section of the PYTHIA8226 tune Monash and ALICE data in proton–proton collisions. Bottom panels show ratio of PYTHIA8226 and ALICE data. The bin sizes between PYTHIA and ALICE data results are different, but the division can be done by doing a linear interpolation for the PYTHIA results.

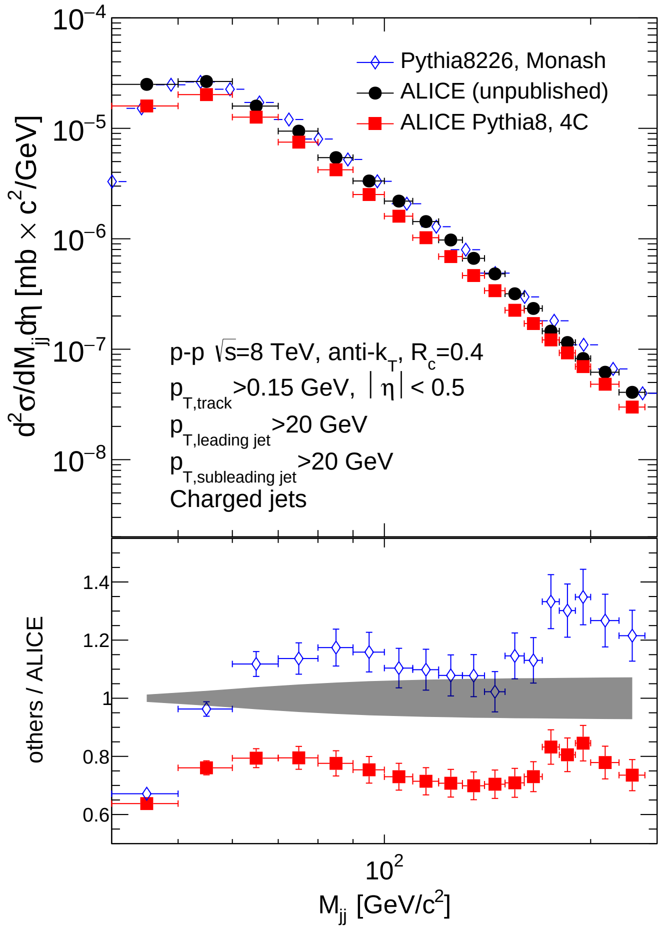

Figure 21. Comparison of Pythia8226, ALICE Pythia8 and unpublished ALICE data [65]. Top panel shows a comparison of the differential charged dijet cross section as a function of the dijet mass in $\sqrt{s} = 8$ TeV proton–proton collisions. Here the $\Delta\phi$ cut has been used for all histograms, which means selecting only dijets with an azimuthal angle of $|\Delta\phi - \pi| < \frac{\pi}{2}$ between the two jets forming the dijet. The $\Delta\phi$ spectra can be seen in figure 17. The bottom panel shows a ratio plot against ALICE data. In the bottom panel the shaded area is the systematic error of the ALICE data.

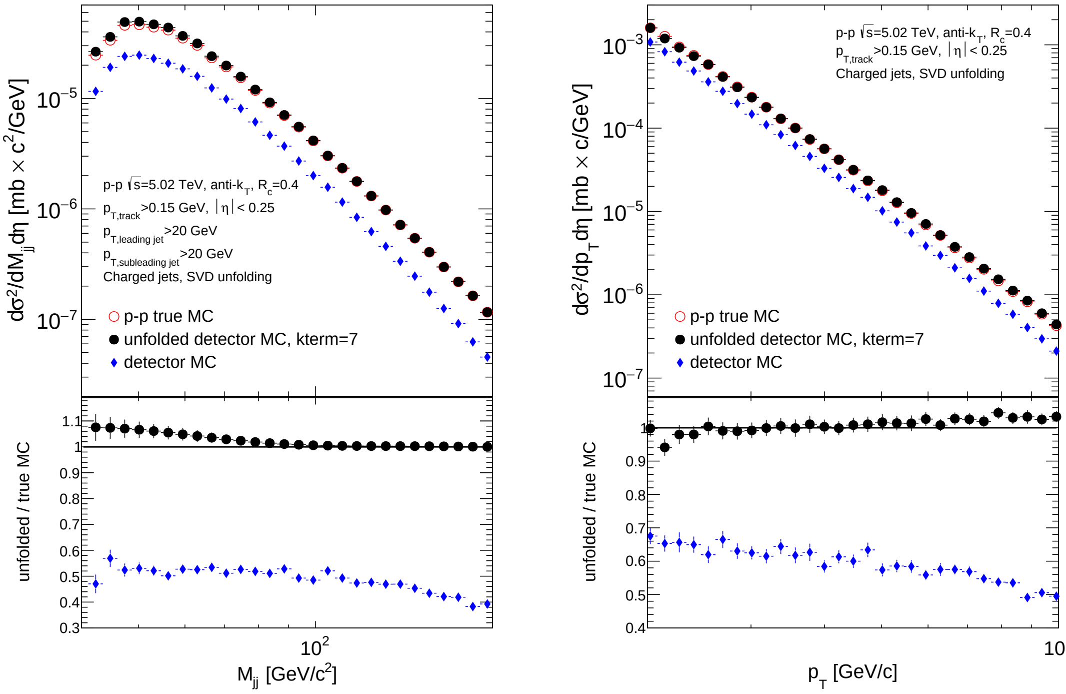

(a) Charged dijet mass cross section. **(b)** Charged jet p_{T} cross section.

Figure 22. Top panel shows the unfolded detector MC in black and the raw detector MC in blue, compared to true MC cross section in red. Bottom panel shows a ratio plot against the true MC. The PYTHIA tune used is Perugia2011.

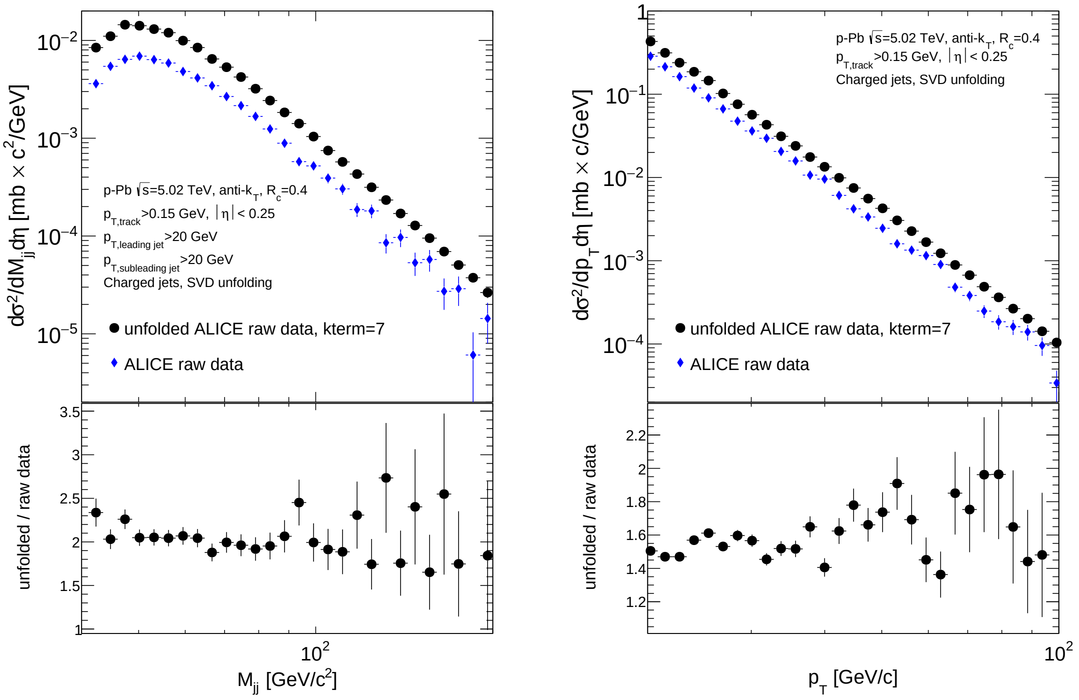

(a) Charged dijet mass cross section.

(b) Charged jet p_{T} cross section.

Figure 23. Top panel shows the unfolded ALICE data in black and the raw ALICE data in blue. Bottom panel shows a ratio against the raw data. In both cases, the unfolding seems to have approximately a constant effect, regardless of the dijet mass or jet p_{T}.

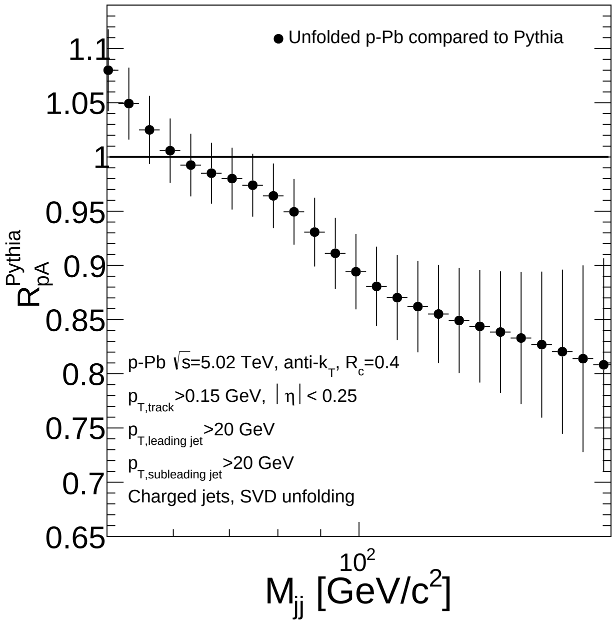

(a) For dijet mass spectrum.

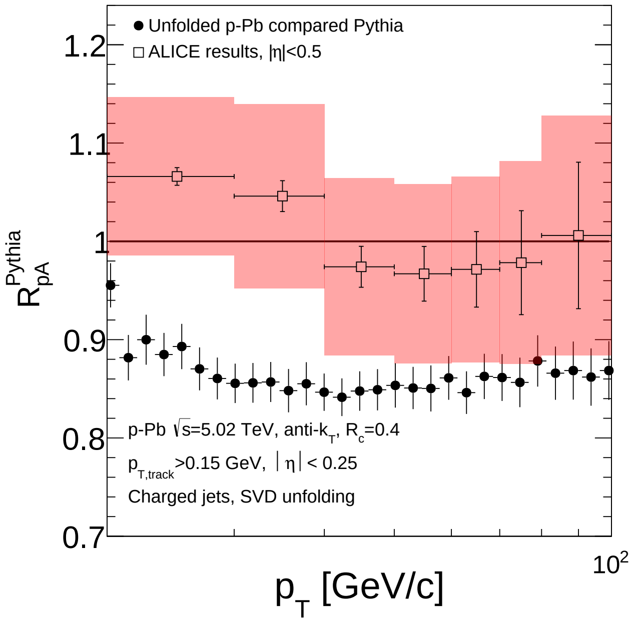

(b) For jet p_T spectrum.

Figure 24. Nuclear modification factor $R_{\mathrm{pA}}^{\mathrm{Pythia}}$ for proton–lead results, which are calculated from 1. The proton–proton reference in this case is the MC truth spectrum presented in figure 22, and the average amount of binary collisions in proton–lead minimum bias collisions $\langle N_{\mathrm{coll}} \rangle = 6.9$ [27]. ALICE results [59] are drawn as a comparison for the jet p_T nuclear modification factor. In addition to statistical errors, also systematic errors have been drawn as red boxes around the ALICE results.

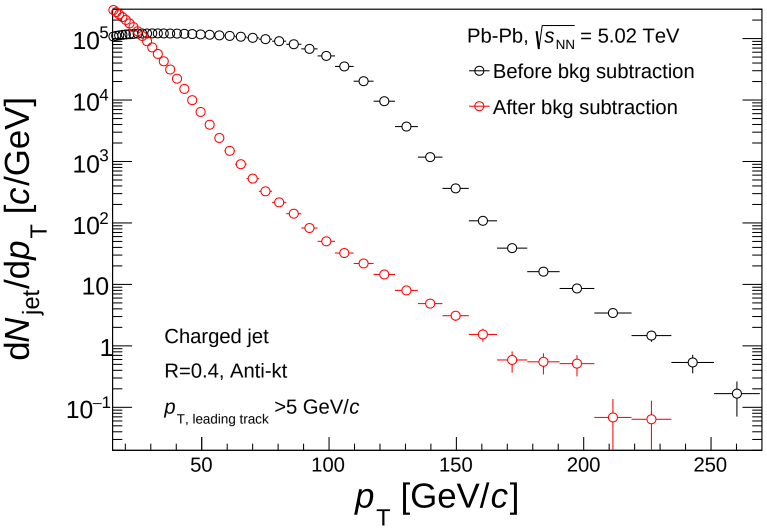

(a) Background subtraction according to equation 27 for lead–lead collisions measured in 2015.

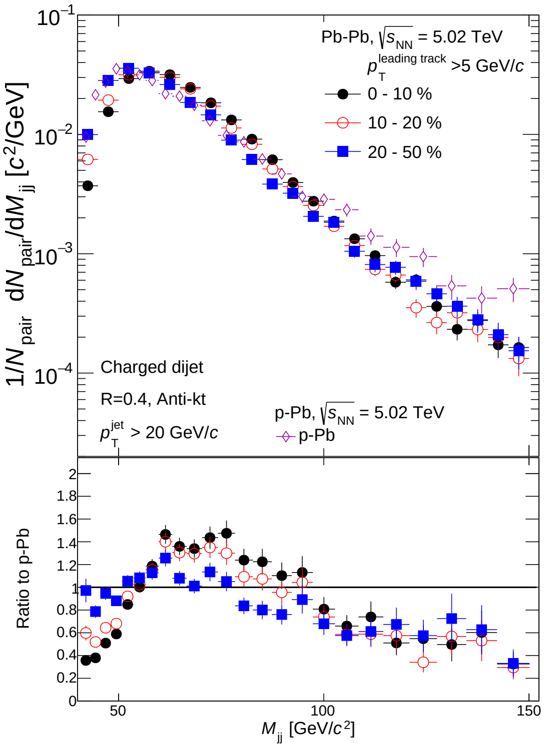

(b) Top panel shows raw dijet mass spectrum in three different centralities in a heavy ion collision after background subtraction according to equation 19, but without an unfolding or embedding study. Also the raw proton–lead results are drawn. Bottom panel shows a ratio of the lead–lead results divided by the proton–lead results.

Figure 25. Lead–lead figures. Here a tighter $\Delta\phi$ cut of $|\Delta\phi - \pi| < \pi/3$ was used for each histogram.

7 Conclusions and outlook

In this thesis I have used proton–proton Monte Carlo and proton–lead ALICE data to test the dijet mass system as a possible probe for quark-gluon plasma in a future study. Proton–lead data unfolding was done with the SVD and Bayesian unfolding, but SVD was primarily used. The unfolding of the dijet mass spectrum presented in this thesis is rather straightforward, and there is room for improvement. Two-dimensional unfolding with dijet mass and dijet transverse momentum together could prove to be even a better unfolding technique which most probably will be tested in the near future. The unfolded proton–lead results were compared to the proton–proton Monte Carlo reference spectrum in figure 24. As the nuclear modification factor for proton–lead is near unity, it would seem that the dijet mass would be usable as a probe in heavy ion collisions as well in the future. The dijet mass comparison between several lead–lead centrality classes and the proton–lead results in figure 25 shows a promising modification for central lead–lead collisions in $M_{\mathrm{jj}} > 100$ GeV. If the modification does preserve through the several corrections and the systematic error is not too large, the dijet invariant mass could very well be used to study QGP in heavy ion collisions.

In order to reach the final goal of finished heavy ion results, several steps need to be taken. As was briefly discussed in chapters 3.2 and 6.3, the unfolding procedure needs to be completed together with the embedding study, in order to counter the jets lost to the background subtraction process. In the study hard jets are embedded in a heavy ion environment and are then unfolded. Another necessary part of the analysis before these results could be published is the calculation of systematic error. Jets are well known in high energy physics so many aspects of the systematic error calculation can be adopted from there, but the dijet system is still new. The heavy ion environment with prominent background could possibly create big systematic uncertainties. In addition, statistics will be a challenge for the dijet study in the heavy ion environment. For example the 2015 heavy ion data used in this thesis had barely enough statistics for the peripheral bins, and they needed to be left out because the high dijet mass bins were too ambiguous.

References

[1] David Griffiths. *Introduction to elementary particles.* 2008. ISBN: 9783527406012.

[2] Y. Aoki et al. ”The Order of the quantum chromodynamics transition predicted by the standard model of particle physics”. In: *Nature* 443 (2006), pp. 675–678. DOI: `10.1038/nature05120`. arXiv: `hep-lat/0611014 [hep-lat]`.

[3] John W. Harris and Berndt Muller. ”The Search for the quark - gluon plasma”. In: *Ann. Rev. Nucl. Part. Sci.* 46 (1996), pp. 71–107. DOI: `10.1146/annurev.nucl.46.1.71`. arXiv: `hep-ph/9602235 [hep-ph]`.

[4] V. A. Kuzmin, V. A. Rubakov, and M. E. Shaposhnikov. ”On the Anomalous Electroweak Baryon Number Nonconservation in the Early Universe”. In: *Phys. Lett.* 155B (1985), p. 36. DOI: `10.1016/0370-2693(85)91028-7`.

[5] Hua Zheng, Jaime Sahagun, and Aldo Bonasera. ”Neutron stars and supernova explosions in the framework of Landau’s theory”. In: *Int. J. Mod. Phys.* E24.07 (2015), p. 1550059. DOI: `10.1142/S0218301315500597`. arXiv: `1411.3030 [nucl-th]`.

[6] Denis Leahy and Rachid Ouyed. ”Supernova SN2006gy as a first ever Quark Nova?” In: *Mon. Not. Roy. Astron. Soc.* 387 (2008), p. 1193. DOI: `10.1111/j.1365-2966.2008.13312.x`. arXiv: `0708.1787 [astro-ph]`.

[7] Aleksi Kurkela and Aleksi Vuorinen. ”Cool quark matter”. In: *Phys. Rev. Lett.* 117.4 (2016), p. 042501. DOI: `10.1103/PhysRevLett.117.042501`. arXiv: `1603.00750 [hep-ph]`.

[8] F. Karsch, K. Redlich, and A. Tawfik. ”Thermodynamics at nonzero baryon number density: A Comparison of lattice and hadron resonance gas model calculations”. In: *Phys. Lett.* B571 (2003), pp. 67–74. DOI: `10.1016/j.physletb.2003.08.001`. arXiv: `hep-ph/0306208 [hep-ph]`.

[9] Henning Kirschenmann. URL: `http://cms.web.cern.ch/news/jets-cms-and-determination-their-energy-scale`.

[10] K. Adcox et al. ”Suppression of hadrons with large transverse momentum in central Au+Au collisions at $\sqrt{s_{\mathrm{NN}}} = 130$ GeV”. In: *Phys. Rev. Lett.* 88 (2002), p. 022301. DOI: `10.1103/PhysRevLett.88.022301`. arXiv: `nucl-ex/0109003 [nucl-ex]`.

[11] C. Adler et al. ”Centrality dependence of high p_T hadron suppression in Au+Au collisions at $\sqrt{s_{\mathrm{NN}}} = 130$ GeV”. In: *Phys. Rev. Lett.* 89 (2002), p. 202301. DOI: `10.1103/PhysRevLett.89.202301`. arXiv: `nucl-ex/0206011 [nucl-ex]`.

[12] Anton Andronic et al. ”Decoding the phase structure of QCD via particle production at high energy”. In: (2017). arXiv: `1710.09425 [nucl-th]`.

[13] Peter Brockway Arnold et al. "Apparent thermalization due to plasma instabilities in quark-gluon plasma". In: *Phys. Rev. Lett.* 94 (2005), p. 072302. DOI: `10.1103/PhysRevLett.94.072302`. arXiv: `nucl-th/0409068 [nucl-th]`.

[14] Philip J. Siemens and John O. Rasmussen. "Evidence for a blast wave from compress nuclear matter". In: *Phys. Rev. Lett.* 42 (1979), pp. 880–887. DOI: `10.1103/PhysRevLett.42.880`.

[15] K. J. Eskola et al. "RHIC-tested predictions for low-p(T) and high-p(T) hadron spectra in nearly central Pb + Pb collisions at the CERN LHC". In: *Phys. Rev.* C72 (2005), p. 044904. DOI: `10.1103/PhysRevC.72.044904`. arXiv: `hep-ph/0506049 [hep-ph]`.

[16] M. H. Thoma. "Damping rate of a hard photon in a relativistic plasma". In: *Phys. Rev.* D51 (1995), pp. 862–865. DOI: `10.1103/PhysRevD.51.862`. arXiv: `hep-ph/9405309 [hep-ph]`.

[17] David d'Enterria. "Jet quenching". In: *Landolt-Bornstein* 23 (2010), p. 471. DOI: `10.1007/978-3-642-01539-7_16`. arXiv: `0902.2011 [nucl-ex]`.

[18] Thorsten Renk and K. Eskola. "Prospects of medium tomography using back-to-back hadron correlations". In: *Phys. Rev.* C75 (2007), p. 054910. DOI: `10.1103/PhysRevC.75.054910`. arXiv: `hep-ph/0610059 [hep-ph]`.

[19] J. Adams et al. "Evidence from d + Au measurements for final state suppression of high p(T) hadrons in Au+Au collisions at RHIC". In: *Phys. Rev. Lett.* 91 (2003), p. 072304. DOI: `10.1103/PhysRevLett.91.072304`. arXiv: `nucl-ex/0306024 [nucl-ex]`.

[20] Brian Dorney. URL: `https://www.quantumdiaries.org/2011/07/09/in-a-world-without-color-why-do-i-believe-in-gluons/`.

[21] S. Acharya et al. "First measurement of jet mass in Pb–Pb and p–Pb collisions at the LHC". In: *Phys. Lett.* B776 (2018), pp. 249–264. DOI: `10.1016/j.physletb.2017.11.044`. arXiv: `1702.00804 [nucl-ex]`.

[22] A. Majumder and J. Putschke. "Mass depletion: a new parameter for quantitative jet modification". In: *Phys. Rev.* C93.5 (2016), p. 054909. DOI: `10.1103/PhysRevC.93.054909`. arXiv: `1408.3403 [nucl-th]`.

[23] Georges Aad et al. "Observation of a Centrality-Dependent Dijet Asymmetry in Lead-Lead Collisions at $\sqrt{s_{\mathrm{NN}}} = 2.77$ TeV with the ATLAS Detector at the LHC". In: *Phys. Rev. Lett.* 105 (2010), p. 252303. DOI: `10.1103/PhysRevLett.105.252303`. arXiv: `1011.6182 [hep-ex]`.

[24] Serguei Chatrchyan et al. "Jet momentum dependence of jet quenching in PbPb collisions at $\sqrt{s_{\mathrm{NN}}} = 2.76$ TeV". In: *Phys. Lett.* B712 (2012), pp. 176–197. DOI: `10.1016/j.physletb.2012.04.058`. arXiv: `1202.5022 [nucl-ex]`.

[25] Georges Aad et al. "Search for New Physics in Dijet Mass and Angular Distributions in pp Collisions at $\sqrt{s} = 7$ TeV Measured with the ATLAS Detector". In: *New J. Phys.* 13 (2011), p. 053044. DOI: `10.1088/1367-2630/13/5/053044`. arXiv: `1103.3864 [hep-ex]`.

[26] Serguei Chatrchyan et al. "Search for Resonances in the Dijet Mass Spectrum from 7 TeV pp Collisions at CMS". In: *Phys. Lett.* B704 (2011), pp. 123–142. DOI: `10.1016/j.physletb.2011.09.015`. arXiv: `1107.4771 [hep-ex]`.

[27] Jaroslav Adam et al. ”Centrality dependence of charged jet production in p–Pb collisions at $\sqrt{s_{\rm NN}} = 5.02$ TeV”. In: *Eur. Phys. J.* C76.5 (2016), p. 271. DOI: `10.1140/epjc/s10052-016-4107-8`. arXiv: `1603.03402 [nucl-ex]`.

[28] Betty Abelev et al. ”Long-range angular correlations on the near and away side in p-Pb collisions at $\sqrt{s_{NN}} = 5.02$ TeV”. In: *Phys. Lett.* B719 (2013), pp. 29–41. DOI: `10.1016/j.physletb.2013.01.012`. arXiv: `1212.2001 [nucl-ex]`.

[29] Betty Bezverkhny Abelev et al. ”Long-range angular correlations of π, K and p in p-Pb collisions at $\sqrt{s_{\rm NN}} = 5.02$ TeV”. In: *Phys. Lett.* B726 (2013), pp. 164–177. DOI: `10.1016/j.physletb.2013.08.024`. arXiv: `1307.3237 [nucl-ex]`.

[30] Jaroslav Adam et al. ”Enhanced production of multi-strange hadrons in high-multiplicity proton-proton collisions”. In: *Nature Phys.* 13 (2017), pp. 535–539. DOI: `10.1038/nphys4111`. arXiv: `1606.07424 [nucl-ex]`.

[31] B. Abelev et al. ”Measurement of charged jet suppression in Pb-Pb collisions at $\sqrt{s_{\rm NN}} = 2.76$ TeV”. In: *JHEP* 1403 (2014), p. 013. DOI: `10.1007/JHEP03(2014)013`. arXiv: `1311.0633 [nucl-ex]`.

[32] Guang-You Qin and Xin-Nian Wang. ”Jet quenching in high-energy heavy-ion collisions”. In: *Int. J. Mod. Phys.* E24.11 (2015). [,309(2016)], p. 1530014. DOI: `10.1142/S0218301315300143,10.1142/9789814663717_0007`. arXiv: `1511.00790 [hep-ph]`.

[33] K. J. Eskola et al. ”The Fragility of high-p(T) hadron spectra as a hard probe”. In: *Nucl. Phys.* A747 (2005), pp. 511–529. DOI: `10.1016/j.nuclphysa.2004.09.070`. arXiv: `hep-ph/0406319 [hep-ph]`.

[34] Betty Abelev et al. ”Underlying Event measurements in pp collisions at $\sqrt{s} =$ 0.9 and 7 TeV with the ALICE experiment at the LHC”. In: *JHEP* 07 (2012), p. 116. DOI: `10.1007/JHEP07(2012)116`. arXiv: `1112.2082 [hep-ex]`.

[35] C. Loizides, J. Nagle, and P. Steinberg. ”Improved version of the PHOBOS Glauber Monte Carlo”. In: *SoftwareX* 1-2 (2015), pp. 13–18. DOI: `10.1016/j.softx.2015.05.001`. arXiv: `1408.2549 [nucl-ex]`.

[36] Betty Abelev et al. ”Centrality determination of Pb-Pb collisions at $\sqrt{s_{\rm NN}} =$ 2.76 TeV with ALICE”. In: *Phys.Rev.* C88.4 (2013), p. 044909. DOI: `10.1103/PhysRevC.88.044909`. arXiv: `1301.4361 [nucl-ex]`.

[37] Torbjörn Sjöstrand et al. ”An Introduction to PYTHIA 8.2”. In: *Comput. Phys. Commun.* 191 (2015), pp. 159–177. DOI: `10.1016/j.cpc.2015.01.024`. arXiv: `1410.3012 [hep-ph]`.

[38] Betty Bezverkhny Abelev et al. ”Charged jet cross sections and properties in proton-proton collisions at $\sqrt{s} = 7$ TeV”. In: *Phys. Rev.* D91.11 (2015), p. 112012. DOI: `10.1103/PhysRevD.91.112012`. arXiv: `1411.4969 [nucl-ex]`.

[39] S. Catani et al. ”Longitudinally invariant K_t clustering algorithms for hadron hadron collisions”. In: *Nucl. Phys.* B406 (1993), pp. 187–224. DOI: `10.1016/0550-3213(93)90166-M`.

[40] Matteo Cacciari, Gavin P. Salam, and Gregory Soyez. ”The Anti-k(t) jet clustering algorithm”. In: *JHEP* 04 (2008), p. 063. DOI: `10.1088/1126-6708/2008/04/063`. arXiv: `0802.1189 [hep-ph]`.

[41] Matteo Cacciari, Gavin P. Salam, and Gregory Soyez. "FastJet User Manual". In: *Eur.Phys.J.* C72 (2012), p. 1896. DOI: `10.1140/epjc/s10052-012-1896-2`. arXiv: `1111.6097 [hep-ph]`.

[42] Gerald C. Blazey et al. "Run II jet physics". In: *QCD and weak boson physics in Run II. Proceedings, Batavia, USA, March 4-6, June 3-4, November 4-6, 1999.* 2000, pp. 47–77. arXiv: `hep-ex/0005012 [hep-ex]`. URL: `http://lss.fnal.gov/cgi-bin/find_paper.pl?conf-00-092`.

[43] J. M. Butterworth et al. "KtJet: A C++ implementation of the K-perpendicular clustering algorithm". In: *Comput. Phys. Commun.* 153 (2003), pp. 85–96. DOI: `10.1016/S0010-4655(03)00156-5`. arXiv: `hep-ph/0210022 [hep-ph]`.

[44] Gregory Soyez et al. "Pileup subtraction for jet shapes". In: *Phys. Rev. Lett.* 110.16 (2013), p. 162001. DOI: `10.1103/PhysRevLett.110.162001`. arXiv: `1211.2811 [hep-ph]`.

[45] Matteo Cacciari, Gavin P. Salam, and Gregory Soyez. "The Catchment Area of Jets". In: *JHEP* 04 (2008), p. 005. DOI: `10.1088/1126-6708/2008/04/005`. arXiv: `0802.1188 [hep-ph]`.

[46] Arpad Horvath. Free to use under CC BY-SA 2.5 license. URL: `https://commons.wikimedia.org/wiki/User:Harp`.

[47] K. Aamodt et al. "The ALICE experiment at the CERN LHC". In: *JINST* 3 (2008), S08002. DOI: `10.1088/1748-0221/3/08/S08002`.

[48] P Cortese et al. "ALICE technical design report on forward detectors: FMD, T0 and V0". In: (2004).

[49] Betty Abelev et al. "Pseudorapidity density of charged particles in p + Pb collisions at $\sqrt{s_{\rm NN}} = 5.02$ TeV". In: *Phys. Rev. Lett.* 110.3 (2013), p. 032301. DOI: `10.1103/PhysRevLett.110.032301`. arXiv: `1210.3615 [nucl-ex]`.

[50] G. L. Bayatian et al. "CMS Physics: Technical Design Report Volume 1: Detector Performance and Software". In: (2006).

[51] PYTHIA *event generator home page.* URL: `http://home.thep.lu.se/Pythia/`.

[52] René Brun et al. "GEANT Detector Description and Simulation Tool". In: (1994). DOI: `10.17181/CERN.MUHF.DMJ1`.

[53] S. van der Meer. "Calibration of the Effective Beam Height in the ISR". In: (1968).

[54] Betty Abelev et al. "Measurement of inelastic, single- and double-diffraction cross sections in proton–proton collisions at the LHC with ALICE". In: *Eur. Phys. J.* C73.6 (2013), p. 2456. DOI: `10.1140/epjc/s10052-013-2456-0`. arXiv: `1208.4968 [hep-ex]`.

[55] Betty Bezverkhny Abelev et al. "Measurement of visible cross sections in proton-lead collisions at $\sqrt{s_{\rm NN}} = 5.02$ TeV in van der Meer scans with the ALICE detector". In: *JINST* 9.11 (2014), P11003. DOI: `10.1088/1748-0221/9/11/P11003`. arXiv: `1405.1849 [nucl-ex]`.

[56] Paolo Nason. "A New method for combining NLO QCD with shower Monte Carlo algorithms". In: *JHEP* 11 (2004), p. 040. DOI: `10.1088/1126-6708/2004/11/040`. arXiv: `hep-ph/0409146 [hep-ph]`.

[57] Stefano Frixione, Paolo Nason, and Carlo Oleari. "Matching NLO QCD computations with Parton Shower simulations: the POWHEG method". In: *JHEP* 11 (2007), p. 070. DOI: `10.1088/1126-6708/2007/11/070`. arXiv: `0709.2092 [hep-ph]`.

[58] Simone Alioli et al. "A general framework for implementing NLO calculations in shower Monte Carlo programs: the POWHEG BOX". In: *JHEP* 06 (2010), p. 043. DOI: `10.1007/JHEP06(2010)043`. arXiv: `1002.2581 [hep-ph]`.

[59] Jaroslav Adam et al. "Measurement of charged jet production cross sections and nuclear modification in p-Pb collisions at $\sqrt{s_{\mathrm{NN}}} = 5.02$ TeV". In: *Phys. Lett.* B749 (2015), pp. 68–81. DOI: `10.1016/j.physletb.2015.07.054`. arXiv: `1503.00681 [nucl-ex]`.

[60] G. D'Agostini. "A multidimensional unfolding method based on Bayes' theorem". In: *Nucl. Instrum. Meth.* A362.2 (1995), pp. 487–498. ISSN: 0168-9002. DOI: `10.1016/0168-9002(95)00274-X`. URL: `http://www.sciencedirect.com/science/article/pii/016890029500274X`.

[61] Volker Blobel. "An Unfolding method for high-energy physics experiments". In: *Advanced Statistical Techniques in Particle Physics. Proceedings, Conference, Durham, UK, March 18-22, 2002.* 2002, pp. 258–267. arXiv: `hep-ex/0208022 [hep-ex]`. URL: `http://www.ippp.dur.ac.uk/Workshops/02/statistics/proceedings//blobel2.pdf`.

[62] Andreas Hocker and Vakhtang Kartvelishvili. "SVD approach to data unfolding". In: *Nucl. Instrum. Meth.* A372 (1996), pp. 469–481. DOI: `10.1016/0168-9002(95)01478-0`. arXiv: `hep-ph/9509307 [hep-ph]`.

[63] Tim Adye. "Unfolding algorithms and tests using RooUnfold". In: *Proceedings, PHYSTAT 2011 Workshop on Statistical Issues Related to Discovery Claims in Search Experiments and Unfolding, CERN,Geneva, Switzerland 17-20 January 2011.* CERN. Geneva: CERN, 2011, pp. 313–318. DOI: `10.5170/CERN-2011-006.313`. arXiv: `1105.1160 [physics.data-an]`. URL: `https://inspirehep.net/record/898599/files/arXiv:1105.1160.pdf`.

[64] Peter Skands, Stefano Carrazza, and Juan Rojo. "Tuning PYTHIA 8.1: the Monash 2013 Tune". In: *Eur. Phys. J.* C74.8 (2014), p. 3024. DOI: `10.1140/epjc/s10052-014-3024-y`. arXiv: `1404.5630 [hep-ph]`.

[65] Beomkyu Kim. Unfolded ALICE data results, however, not published yet. 2017.

A Appendix

A.1 Double differential cross section for Monte Carlo

The equation 33 describes the double differential cross section for ALICE data, but for the MC the procedure is a bit different. The power law behavior of the transverse spectra is known, and can be seen in the figures of this thesis also. This means that high p_T phenomena are exceedingly rare and require enormous amounts of events for decent statistics. MC simulations would need to be ran months or even years if one would like to study high p_T physics. Fortunately there is a way to counter this for MC simulations. MC generators can be set to produce high p_T jets in every event and then this can be scaled appropriately. This setting is generally called $p_\mathrm{T,hard}$, and by setting a range to $p_\mathrm{T,hard}$ the generator will produce only high energy partons in that p_T range, according to equation 4. These results need then to be scaled by $\sigma_\mathrm{gen}/N_\mathrm{accepted}$, where σ_gen is the estimated cross section summed over all allowed processes in millibarns, and N_accepted is the total number of accepted events. This way the real cross section can be calculated even with $p_\mathrm{T,hard}$ restrictions. The double differential cross section for MC results is written as

$$\frac{\mathrm{d}^2\sigma}{\mathrm{d}p_\mathrm{T}\mathrm{d}\eta} = \frac{1}{\mathcal{L}}\frac{\Delta N}{\Delta p_\mathrm{T}\Delta\eta} = \frac{\sigma_\mathrm{gen}}{N_\mathrm{accepted}}\frac{\Delta N}{\Delta p_\mathrm{T}\Delta\eta}, \tag{37}$$

where $\mathcal{L}$ is the luminosity, ΔN number of hits in a certain p_T bin, Δp_T is the width of the bin and $\Delta\eta$ is the total size of pseudorapidity acceptance. In this work I have used this to run several different MC runs with different $p_\mathrm{T,hard}$ ranges. In figure 26 I have plotted the individual $p_\mathrm{T,hard}$ bins for three energies, 8 TeV, 7 TeV and 5.02 TeV, and the sum of all the bins, which represents the jet cross section.

A.2 Additional Monte Carlo jet p_T figures

The comparison of two different Pythia tunes can be seen for jets and dijets in $\sqrt{s} = 8$ TeV proton–proton collisions in figure 27. In the shown range, the difference in spectra can be up to 25 %, which is surprisingly large. On the other hand, in figures 28 and 29 comparisons between $\sqrt{s} = 7$ TeV and $\sqrt{s} = 8$ TeV jet p_T spectra are shown. For figure 28 the 7 TeV results were achieved with the Pythia6 tune Perugia0, and the 8 TeV results with the Pythia8 tune 4C. Then three powerlaw fits of the form

$$\frac{\mathrm{d}\sigma^2}{\mathrm{d}p_\mathrm{T}\mathrm{d}\eta}(p_\mathrm{T}) = Cp_\mathrm{T}^{-n}$$

were fitted to each result, which clearly shows how the exponent of the fit grows larger in the high p_{T} region. The bending is not nearly as prominent in every PYTHIA tune. In figure 29 several different 7 TeV versus 8 TeV comparisons are made, where the spectrum can be seen behaving in different ways in the high p_{T} region. Some of the spectra bend seemingly less than others. When comparing the two energies in figure 29, a similar rise in the high p_{T} region on the ratio plot can be seen in both the ALICE PYTHIA results and in the stand alone PYTHIA8226 production. In the ALICE data the rise is not seen so conclusively, but 8 TeV still has constantly higher yields than 7 TeV.

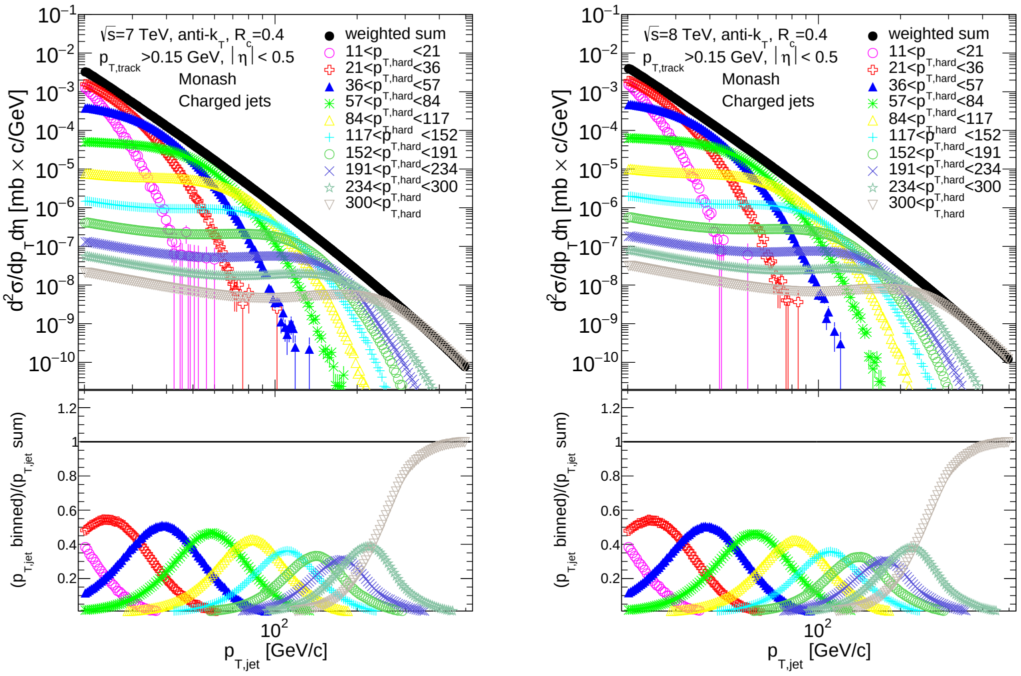

(a) $\sqrt{s} = 7$ TeV **(b)** $\sqrt{s} = 8$ TeV

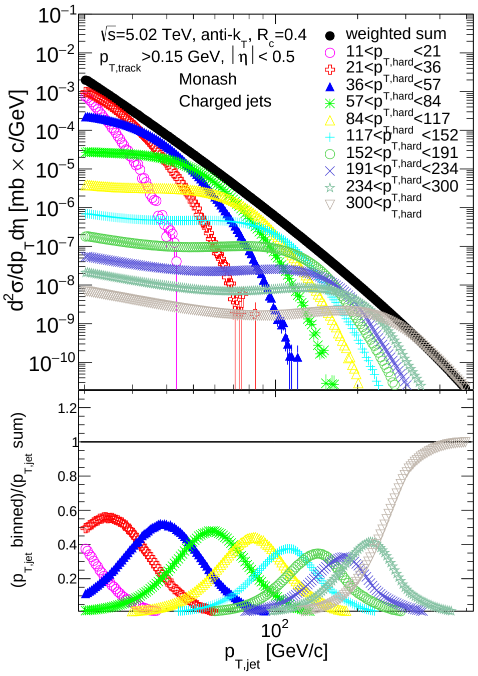

(c) $\sqrt{s} = 5.02$ TeV

Figure 26. Top panels show charged jet cross sections in proton–proton collisions plotted in $p_{\mathrm{T,hard}}$ bins. PYTHIA8226 tune Monash was used in each run. In black the total summed up histogram is the total charged jet cross section. Bottom panel shows the ratio of the binned cross sections and the total cross section.

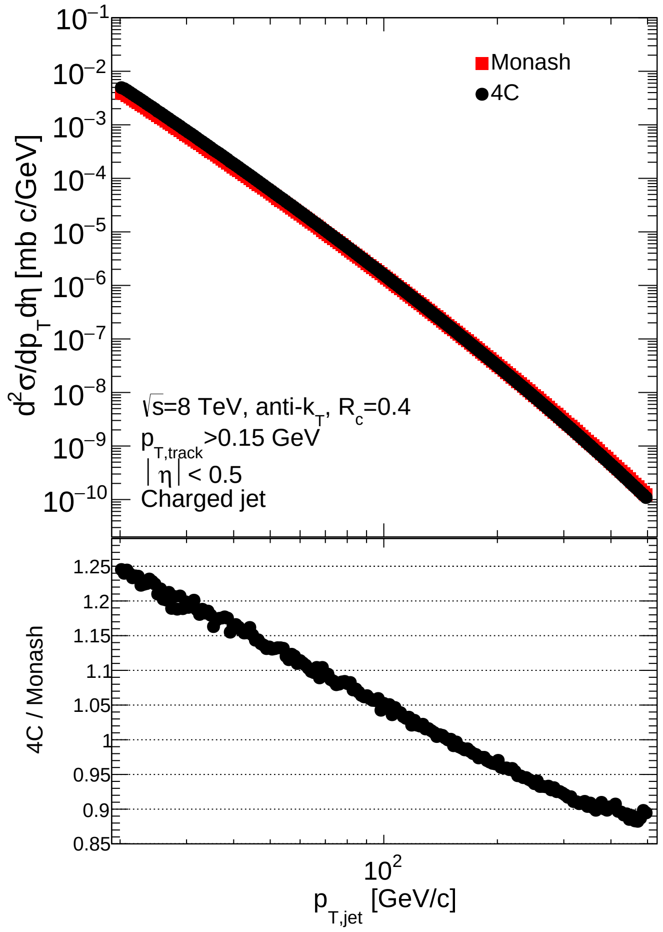

Figure 27. Event generator tune comparison for the charged jet cross sections in $\sqrt{s} = 8$ TeV in proton–proton collisions. Top panel shows the tunes Monash and 4C. Bottom panel shows the 4C results divided by the Monash results.

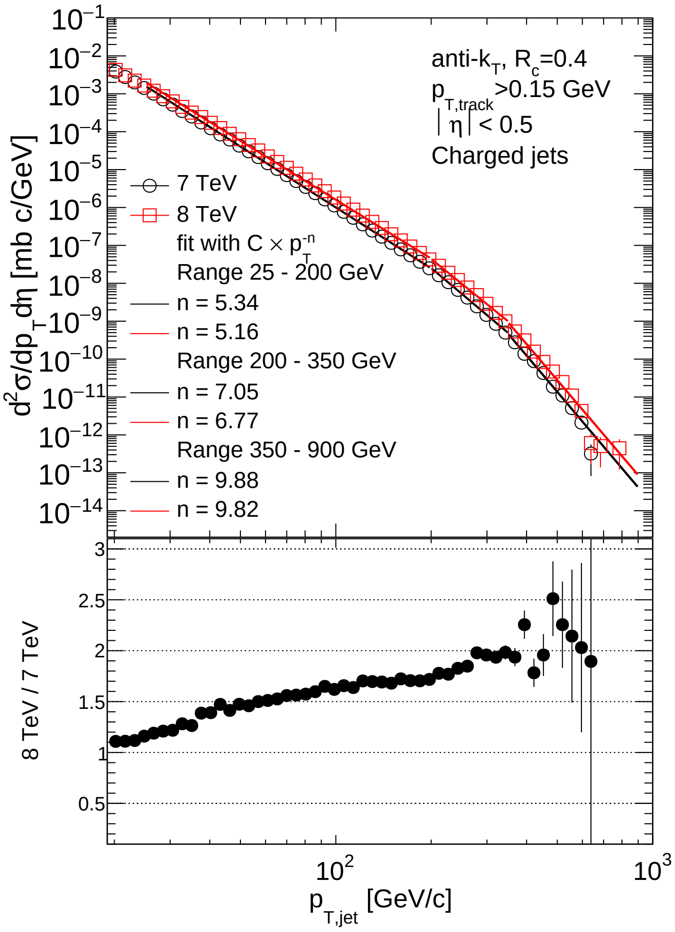

Figure 28. Top panel shows charged jet cross section comparison between the 7 TeV Pythia6 tune Perugia0 and the 8 TeV Pythia8 tune 4C. Three polynomial fits are plotted also with varying fit sections. Bottom panel shows the ratio of the 8 TeV and 7 TeV histograms.

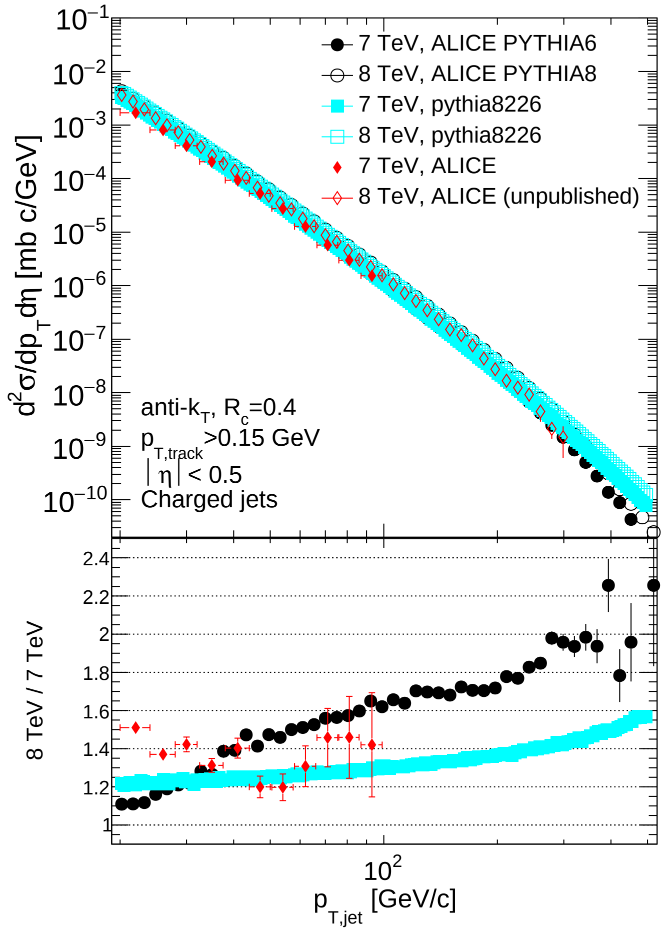

Figure 29. Top panel shows charged jet cross section comparisons between Pythia8226, ALICE Pythia and ALICE data in $\sqrt{s} = 7$ TeV and 8 TeV proton–proton collisions. Bottom panel shows the ratio plot of the 7 TeV divided by the 8 TeV results for each tune.